

Relating Multivariate Shapes to Genescapes Using Phenotype-Biological Process Associations for Craniofacial Shape

October 20, 2021

J. David Aponte¹, David C. Katz¹, Daniela M. Roth², Marta Vidal Garcia¹, Wei Liu¹,
Fernando Andrade³, Charles C. Roseman³, Stephen A. Murray⁵, James Cheverud³,
Daniel Graf^{2,6}, Ralph S. Marcucio⁷, Benedikt Hallgrímsson^{1*}

¹ Department of Cell Biology & Anatomy, Alberta Children's Hospital Research Institute and
McCaig Bone and Joint Institute, Cumming School of Medicine, University of Calgary, Calgary
AB, Canada

² School of Dentistry, Faculty of Medicine and Dentistry, University of Alberta, Edmonton, AB,
Canada

³ Department of Biology, Loyola University Chicago, Chicago, IL, USA

⁴ Department of Animal Biology, University of Illinois Urbana Champaign, Urbana, IL, USA

⁵ The Jackson Laboratory, Bar Harbor, ME, USA

⁶ Department of Medical Genetics, Faculty of Medicine and Dentistry, University of Alberta,
Edmonton, AB, Canada

⁷ Department of Orthopaedic Surgery, School of Medicine, University of California San
Francisco, San Francisco, CA, USA

Words: 7697

Figures: 10

Abstract

Realistic mappings of genes to morphology are inherently multivariate on both sides of the equation. The importance of coordinated gene effects on morphological phenotypes is clear from the intertwining of gene actions in signaling pathways, gene regulatory networks, and developmental processes underlying the development of shape and size. Yet, current approaches tend to focus on identifying and localizing the effects of individual genes and rarely leverage the information content of high dimensional phenotypes. Here, we explicitly model the joint effects of biologically coherent collections of genes on a multivariate trait—craniofacial shape—in a sample of $n = 1,145$ mice from the Diversity Outbred (DO) experimental line. We use biological process gene ontology (GO) annotations to select skeletal and facial development gene sets and solve for the axis of shape variation that maximally covaries with gene set marker variation. We use our process-centered, multivariate genotype-phenotype (process MGP) approach to determine the overall contributions to craniofacial variation of genes involved in relevant processes and how variation in different processes corresponds to multivariate axes of shape variation. Further, we compare the directions of effect in phenotype space of mutations to the primary axis of shape variation associated with broader pathways within which they are thought to function. Finally, we leverage the relationship between mutational and pathway-level effects to predict phenotypic effects beyond craniofacial shape in specific mutants. We also introduce an online application which provides users the means to customize their own process-centered craniofacial shape analyses in the DO. The process-centered approach is generally applicable to any continuously varying phenotype and thus has wide-reaching implications for complex-trait genetics.

Keywords: multivariate genotype-phenotype map, complex traits, mouse, craniofacial, diversity
outbred

Introduction

Variation in human craniofacial shape is moderately to highly heritable (~30-70% (Cole et al., 2017; Tsagkراسoulis et al., 2017)), and resemblances among close relatives as well as twins underscore the strong relationship between shared genetics and shared phenotype (Johannsdottir et al., 2005; Nakata, 1985). Despite many studies in humans and in mice (Claes et al., 2018; Cole et al., 2016; Shaffer et al., 2016), however, we know very little about the genetic basis for variation in craniofacial shape. This is likely due to genetic complexity (Katz et al., 2019; Richtsmeier and Flaherty, 2013; Visscher, 2008; Wood et al., 2014; Wray et al., 2013). Like many aspects of morphological variation, craniofacial shape is extraordinarily polygenic. Genes with major mechanistic roles in facial development such as *Fgf8* often contribute little to observed phenotypic variation (Green et al., 2017) while genetic influences without obvious connections to craniofacial development emerge as significant contributors (Kenney-Hunt et al., 2008; Klingenberg and Leamy, 2001; Maga et al., 2015; Pallares et al., 2015, 2014). The effects of genetic variants on phenotype often depend on genetic background (Mackay and Moore, 2014; Percival et al., 2017) and many mutations have variably penetrant effects even when background is controlled (Hallgrimsson et al., 2009; Rendel, 1967). These issues likely arise because genetic influences act through multiple layers of interacting developmental processes to influence phenotypic traits, resulting in complex patterns of epistasis and variance heterogeneity (Hallgrimsson et al., 2018, 2014; Kawauchi et al., 2009; Wagner and Zhang, 2011). Solutions that go beyond studies of single gene effects are required to overcome these significant challenges in complex-trait genetics. Here, we implement an enhanced form of the more general candidate gene approach to evaluate the conjoint effects of multiple genes on a complex trait – craniofacial shape.

There are two basic approaches to mapping genetic effects on to phenotypic variation. A candidate gene approach measures genotypic values with known physiological and biochemical relationships to the phenotypes of interest (Cheverud and Routman, 1993). In contrast, a random marker or genome-wide approach seeks to associate any potential genetic variant with variation

in the trait of interest. There are advantages and disadvantages to these two approaches. The candidate gene approach is blind to the unknown – phenotypic variation is often associated with genes not expected to be important. On the other hand, a candidate gene approach allows direct measurement of genotypic values and produces results that are interpretable in terms of trait physiology or development. A genome-wide or random marker approach can produce unexpected insight by revealing novel gene-phenotype associations. However, this comes at a great cost in power (Visscher et al., 2017). For highly polygenic traits, this approach often produces a “tip of the iceberg” effect in which studies reveal a small and often incoherent subset of the genes that actually determine variation in the trait of interest (Broman and Sen, 2009, p. 123-124).

Several strategies have been developed that partially overcome these tradeoffs. One solution is the use of polygenic risk scores. Polygenic risk scores assess the overall genetic influence on a trait without regard to the genome-wide significance of individual SNP effects (Dudbridge, 2013; Wray et al., 2007). Approaches such as meta-analyses of genome-wide association studies (GWAS) or studies based on extreme phenotypes (Morozova et al., 2015) have expanded gene lists for a variety of complex traits. However, lengthy lists of genes or overall genomic risk for specific phenotypes do not necessarily constitute tractable genetic explanations for phenotypic variation. When 1000s of genes are required to explain heritable variation in stature, for instance, it is not clear what such lists tell you beyond the obvious fact that stature is heritable and polygenic (Yang et al., 2010; Wood et al., 2014). This tension between hypothesis-driven and hypothesis-free approaches and their attendant tradeoffs between statistical power and interpretability is, arguably, a major issue within complex trait genetics. To resolve this conceptual conflict, approaches are needed that integrate quantitative genetics with biological insights regarding the cellular and developmental processes through which genes influence phenotypic variation.

Existing approaches to complex trait genetics also tend to treat phenotypic traits as singular and one-dimensional. Even for morphological variation, most studies reduce shape variation to linear distances, principal components, regression scores or measures of size which are then mapped as individual traits (Xiong *et al.* 2019; Shaffer et al, 2016; Cole et al, 2016).

This approach disregards the information content of multivariate phenotypic variation. While univariate traits only vary along one dimension, high dimensional traits such as craniofacial shape can vary in direction as well as magnitude within a multi-dimensional shape space. To identify the distinctive axes of gene effects on a multivariate trait, one must model such multiple multivariate relationships directly.

Building on Mitteroecker *et al.*'s (2016) multivariate genotype-phenotype (MGP) method, we extend the candidate-gene framework to evaluate the combined contributions of genes to variation in high-dimensional phenotypic traits such as craniofacial shape. Grouping genes by ontological information such as membership in developmental pathways or other relevant biological hypotheses, our process-centered multivariate approach, herein referred to as process MGP, brings traditional GWAS together with a simplified model of the hierarchical genotype-phenotype (GP) map. Gene ontology terms are broadly grouped into three categories—cellular components, molecular functions, and biological processes. Our work focuses on biological process gene annotations because they group known relationships between several genes that contribute to a developmental function. The process MGP approach aims to leverage this knowledge by modeling the joint effects of these genes on craniofacial shape variation.

Understanding the genetic determinants of craniofacial variation, as with most complex traits, represents a many-to-many genotype-phenotype map problem (Lewontin, 1975). Both phenotypic and genotypic measurements have complex within-set covariance structures. On the genetic side, the covariance structure is represented by pathway/biochemical interactions, as well as chromosomal structure like linkage, chromatin, and 3D chromosomal organization. For shape-related phenotypes, the covariance matrix is structured by the chosen set of landmarks and their resulting coordinates. The functional relationship from genotype to phenotype is then described by a between-set covariance (Klingenberg and Leamy, 2001; Mitteroecker *et al.*, 2016). To dissect these relationships, we use a regularized partial least squares (PLS) (Lorenzo *et al.*, 2019) approach to estimate a low-dimensional mapping from the alleles in our sample to variation in adult mouse craniofacial shape. While PLS is well suited for analysis of covariation between two sets of measurements, regularization is essential for mitigating overfitting when there are many alleles simultaneously modelled. We focus on how allelic variation in processes relevant to

craniofacial development maps to craniofacial shape variation. We ask the following four questions:

- 1) How much shape variation is communally accounted for by genes contributing to a process, e.g., chondrocyte differentiation?
- 2) How similar are the effects of different processes on shape? For instance, do cell proliferation genes affect face shape in a similar way to genes in the bone morphogenetic protein pathway?
- 3) How similar are mutant model effects and process effects? For example, do chondrocyte mutant effects align with the effects of natural variants in chondrocyte differentiation genes?
- 4) Can one use the similarity of a mutational effect to MGP process effects predict unobserved phenotypes associated with that mutation?

Together, these questions demonstrate the ability of the process MGP approach to add meaningful understanding of the complex relationships between genotype and phenotype by quantifying higher level regularities between complex phenotypic and genomic data. We also demonstrate its potential as a resource for the study of mutational effects on complex traits such as craniofacial shape.

Results

Process Multivariate Genotype-Phenotype (MGP) Mapping

For process MGP analyses, we used the mouse genome informatics database (Bult et al., 2018) to identify genes annotated to a given process. Each annotation term has an associated GO ID. For example, “chondrocyte differentiation” has GO ID GO:000206 (Figure 1, box 1). We cross-reference the GO ID with the Ensemble genome database (GRCm38.p6) to find the name, chromosome, and base pair start/end position for each gene (Figure 1, box 2) annotated to the process. For genes with multiple splice variants, we select the longest transcript. For each gene, we compare marker base pair positions and select the closest upstream and downstream markers to the center of each gene. The 8-state genotype probability is then calculated as the average founder allele probabilities between the two selected markers. (Figure 1, box 3). After marker selection, we fit a regularized PLS model using the founder allele probabilities (8 variables/marker) and full landmark data set (Figure 1, box 4). Regularization penalizes the coefficients such that increasing regularization strength causes more coefficients to have a value of zero. We chose a regularization parameter using 10-fold cross validation. For each of the example process MGP analyses shown, we chose the regularization strength that best represented the tradeoff between minimizing model error and maximizing interpretability of marker effects and the similarity of phenotypic effects with mouse mutant models. The full cross validation results are shown in Figures 2, 4, and 5—figure supplement 1.

We demonstrate process MGP mapping with three examples. The first estimates the primary axis of skull shape covariation with genes annotated to “chondrocyte differentiation” (Figure 2). Differentiation of chondrocytes is one of several key developmental processes involved in endochondral ossification. Endochondral bones form the majority of the cranial base through a cartilage model of bone formation (Percival and Richtsmeier, 2013). There are 38 genes annotated to chondrocyte differentiation in the Ensembl database (Yates et al., 2020). In the figure, genetic effects are shown as zero-centered bars that span the range of estimated allele effects across the 8 DO founders; individual founder allele effects—8 per marker—are color-coded within those bars (Figure 2A). We chose a regularization parameter of .075 for this

analysis (Figure 2— figure supplement 1). Among chondrocyte differentiation genes, *Nov/Ccn3*, *Bmpr1b* (*Alk6*), and *Nfib* and are most implicated in the major axis of pathway covariation with craniofacial shape. The phenotypic effects at each landmark primarily relate to antero-posterior positioning of the zygomatic arches and dorso-ventral jugal position (Figure 2B). The chondrocyte differentiation GP map explains 2.15% of the total variance in craniofacial shape. Compared to 10000 random permutations of the model, chondrocyte differentiation explains substantially more craniofacial variation (Figure 2— figure supplement 2).

Figure 2C compares the direction of the chondrocyte differentiation MGP axis— magnified 4x— to the axis of shape variation of a relevant mutant phenotype. We chose homozygous *Bmpr1b* mutants for this comparison for three reasons. The first is because *Bmpr1b* in synergy with other bone morphogenic protein pathway receptors regulates chondrocyte proliferation and differentiation in embryonic cartilage condensations (Yoon et al., 2005). The second reason we chose *Bmpr1b* mutant comparisons is because the marker selected for *Bmpr1b* in the genomic analysis contains one of the strongest allelic effects associated with the morphological effect. *Bmpr1b* shows stronger loading/association than *Bmpr1a* (Fig. 2A). While *Bmpr1a* has well-established roles in craniofacial development (Liu et al. 2005; Liu et al. 2018), the role for *Bmpr1b* on its own is less clear. *Bmpr1b* mutants show shorter long bones at birth and overexpression of a dominant negative *Bmpr1b* using a type 1 collagen promoter showed delayed ossification of the frontal, parietal, and occipital bones (Yoon et al., 2005; Zhao et al., 2002). The overall phenotypic directions of *Bmpr1b* mutant variation and chondrocyte differentiation variation are moderately correlated at $r = 0.371$ ($t = -5.06$, $df = 160$, $p < .0001$), but the direction at landmarks with large effects in mutant and MGP are clearly coincident. Over the landmarks we measured, the chondrocyte differentiation effect is less global than the *Bmpr1b* effect, likely due to the difference in severity of the mutant phenotype.

The similarity of the chondrocyte differentiation effect with the *Bmpr1b* mutant and the high loading *Bmpr1b* allele in the DO genome suggests that *Bmpr1b* mutants may produce chondrocyte differentiation defects in the developing neurocranium. In response to the process MGP results, quantified cell size and distribution in the intersphenoid synchondroses (ISS) of several mutant and control *Bmpr1b* mice (Figure 3—figure supplement 1). We found that

homozygotes show overall larger cell sizes as well as a differing distribution of cell sizes throughout the width of the ISS (Figure 3A-C; $\chi^2 = 21.23$, $df = 3$, $p < .0001$). The presence of larger cell sizes in the homozygote *Bmpr1b* mutants suggests that the synchondroses possess more hypertrophic chondrocytes. Additionally, *Bmpr1b* homozygous mutant mice show premature fusion of the coronal suture (Figure 3D). Both features have not been reported in the literature.

The second example quantifies cranial shape covariation with the 81 genes annotated to “determination of left/right symmetry”. We used a regularization parameter of .04 (Figure 4—figure supplement 1). There are several high loading alleles that contribute to the determination of left/right symmetry MGP phenotype. In particular, an *Fgf10* allele inherited from the Castaneus founder background was among the most important (Figure 4A). FGF10 is a key ligand in early development, directing proliferation as well as differentiation for many craniofacial components, including the palate, teeth, and bones (Hilliard et al., 2005; Prochazkova et al., 2018; Watson and Francavilla, 2018). The phenotype associated with left/right symmetry alleles is predominately related to a larger neurocranium volume relative to the outgrowth of the face (Figure 4B). We also visualized the asymmetry in the phenotypic response, which shows subtle asymmetry, particularly in the position of the anterior zygomatic landmark (Figure 4D). Several Fgf ligands including *Fgf10* are integral in the asymmetric distribution of organs (Hecksher-Sørensen et al. 2004). *Fgf8* has also previously been shown to produce asymmetric craniofacial phenotypes in zebrafish, but craniofacial asymmetry has not previously been observed in *Fgf10* mutants (Albertson & Yelick 2005). Left/right symmetry loci explain 3.4% of the total variance in craniofacial shape, which exceeds the variance explained by 10000 randomly permuted L/R symmetry MGP analyses (Figure 4—figure supplement 2). We compared the estimated L/R symmetry MGP effect with the direction of an *Fgf10* homozygous mutant because of the relative importance of the allelic effect (Figure 4C). The vector correlation between the *Fgf10* mutant and the estimated left/right symmetry effect is 0.672 ($t = 12.29$, $df = 160$, $p < .0001$). The importance of other Fgf ligands in craniofacial symmetry, as well as the high-loading *Fgf10* allele for left/right symmetry MGP along with the similar genomic and mutant phenotypes suggests that *Fgf10* mutants could show directional asymmetry in the cranium. To test this hypothesis, we measured a sample of 8 *Fgf10* adult mutant crania for object

symmetry and detected significant directional asymmetry (Figure 4D; $F = 4.91$, $df = 52$, $p < .0001$).

The final example estimates the shape covariation attributed to the 73 genes annotated to “palate development.” Formation and fusion of the palatal shelves are crucial for proper orofacial development and heavily influences overall facial shape (Greene and Pisano, 2010). We used a regularization penalty of .05 because it best balances the vector correlation to the mutant comparison and the reduction of prediction error (Figure 5—figure supplement 1). Several genes contribute strongly to the palate development MGP effect including *Ephb2*, *Gli3*, and *Lrp6* (Figure 5A). The estimated phenotype shows corresponding variation in palate length as well as strong effects in the majority of the cranial base landmarks (Figure 5B). Palate development MGP loci explain 2.4% of the total variance in cranial shape, which is greater than variance explained by 10000 randomly permuted palate development MGP models (Figure 5—figure supplement 2). We compared the palate development phenotype to a heterozygous *Ankrd11*, neural-crest specific knockout mouse. The *Ankrd11* locus is associated with KBG syndrome in humans, which presents with generally delayed bone mineralization as well craniofacial characteristics including palate abnormalities (Low et al., 2016). While the vector correlation between the palate development MGP effect and the *Ankrd11* mutant over the complete set of cranial landmarks is moderate at $r = .339$ (Figure 5C; $t = 4.31$, $df = 160$, $p = .0001$), the vector correlation for palate landmarks is substantially higher at $r = .536$.

In each case above, we have shown how association of gene sets and phenotypic variation can produce highly informative results that can guide subsequent hypothesis testing. For a given biological process, we identified several genes that load strongly on the primary axis of MGP covariation for which mutant samples were available to us, as well. Future investigations could also use this information about genes with high loadings to generate new mutants for analysis of associated developmental processes. For each example, we focus only on the first PLS axis, so distinct joint gene effect combinations may contribute to novel phenotypic directions in lower PLS axes.

Joint versus single loci effects

While the process MGP approach focuses on the joint effect of markers on craniofacial shape, it is important to measure the extent that joint effects matter for craniofacial shape. Unlike alternative models such as canonical correlation analysis (CCA), the PLS model used for process MGP does not allow for statistical tests of individual marker effects. However, it is possible to measure the similarity of phenotypic effects after successively removing the most heavily loading markers from the full model. Figure 6 shows the change in variance explained (A) as well as the change in the direction of phenotypic response (B) as markers are increasingly removed from the model. For each example analysis, we remove markers in order from most heavily loaded to least heavily loaded. We found that process MGP analyses with few loci of very large effect, like *Ccn3/Nov* for chondrocyte differentiation MGP, are very sensitive to the removal of the most highly loaded genes. The vector correlation between the full chondrocyte differentiation MGP model and the model with the *Ccn3/Nov* marker removed is .346.

For process MGP analyses with a more uniform distribution of marker effects, we found that the phenotypic effect is much more reliant on a multitude of marker alleles. For instance, L/R symmetry MGP with the 10 most heavily loaded markers removed still produced a vector correlation of .95 with the full model. The majority of process MGP analyses demonstrate a similar importance to several alleles, highlighting the main strength process-level analyses over individual marker tests (Figure 6 – figure supplement 1). In the next sections we will examine how process MGP phenotypes relate to each other, as well as the phenotypic directions of several mutant mouse models.

Pairwise comparison of craniofacial development processes

We chose 15 processes integral to craniofacial development and compared the pairwise similarity of effect on craniofacial shape using a heatmap based on clustering of the correlation matrix (R core team, 2017). Processes with similar effects on craniofacial shape will be highly correlated, while processes that affect distinct aspects of craniofacial variation will be uncorrelated to each other. The clustering algorithm resulted in two main blocks of strongly correlated effects (Figure 7A). The largest block of highly correlated phenotypic effects includes

neural crest cell migration, epithelial to mesenchymal transition, forebrain development, as well as some of the most general developmental processes like cell proliferation, bone development, apoptosis, A/P pattern specification, and FGFR signaling. In addition, there is a general BMP block, with Bmp signaling, dorsoventral pattern formation, endochondral ossification, and positive regulation of skeletal muscle tissue growth. Interestingly, phenotypic variation associated with cranial suture morphogenesis, neural tube patterning, and intramembranous ossification is largely uncorrelated with the other craniofacial developmental processes included here.

To assess the stability of the clustering result, we estimated the vector correlation between the cluster distances—also known as the cophenetic distance—and the original correlation matrix (Sneath & Sokal, 1973). A high vector correlation suggests reliable clustering, whereas a low correlation suggests a random clustering result. The correlation between the cophenetic distance matrix and the correlation matrix is 0.648 ($t = 8.64$, $df = 103$, $p = 7.6 \times 10^{-14}$), suggesting a moderate, though significant structure in the similarity of effects amongst this set of MGP processes.

The similarity in process MGP effects suggests that processes may coordinate in a limited set of potential directions of phenotypic variation. One reason that we could observe this pattern that is not because of common axes of genotype-phenotype variation is that key genes show up repeatedly within processes and largely drive these patterns of phenotypic variation. Figure 7B shows over 45,000 pairwise process MGP vector correlations as a function of the number of shared genes between the two randomly chosen annotations. While the similarity of phenotypic effects generally increases as the number of shared genes increases, gene ontology processes that share genes are not necessarily strongly correlated. For gene ontology processes that share between 0 and 10 genes, the observed correlations in phenotypic response spanned from no correlation to almost entirely concordant. Gene ontology processes that share more than 10 genes show generally higher vector correlations, with the lowest vector correlation we observed at .35.

Process effects in the mutant morphospace

To assess the extent to which craniofacial shape variation associated with developmental processes aligns with variation from mutants of major effect, we projected 7 process effects onto the first two principal components (PCs) of a dataset containing the DO sample, and samples from 30 mutant genotypes (Figure 8A). Each black label represents the mean shape score of the listed mutant genotype. The shaded ellipse with an orange border displays the 95% data ellipse of PCs 1 and 2 of DO cranial shape variation. The DO mean shape is contrasted by the mutant variation along PC1. The first PC describes vault size relative to the length of the face. The phenotype shown along the x-axis of figure 8A depicts the maximum positive PC1 shape, while the heatmap drawn on the crania represents the local deformations towards the minimum PC1 shape. The positive direction of PC2 describes coordinated variation that includes a relatively wider vault, narrower zygomatic, and shorter premaxilla (Figure 8A, y-axis margin).

Process effects—highlighted with orange vectors originating at the DO mean shape—are necessarily of smaller magnitude than the total variation in the DO sample. Therefore, to better compare the direction of process effects the vector magnitudes were magnified 4x. Several process effects align in distinct directions of mutant effects, such as bmp signaling pathway and endochondral ossification in the direction of *Shh*, *Nipbl*, and *Ift88* mutants. Neurotransmitter transport and Wnt signaling pathway is similar in direction to *Kcna1*^{Mceph} and *B9d1* mutant effects. Execution phase of apoptosis and intracellular transport both show similar effects to a cluster of Bmp mutants. Figure 8A focuses on two principal components, which allows for the contextualization of how process MGP analyses and mutants vary in similar directions and allows us to visualize what those phenotypes look like. This combination of context and visualization is only possible in limited axes and cannot account for differences or similarities in the full multivariate shape space.

To show the similarity of process MGP directions with mutants in the full shape space, we present a heatmap of 30 process MGP effects to 30 mouse mutant models in figure 8B. The heatmap shows the correlation in direction with yellow/green denoting higher correlation and teal/blue denoting lower correlation. The bottom right of the heatmap (highlighted by a white border) shows a block of mutants for which there are strong process correlations. These are among the most extreme phenotypes along PC1 (Figure 8A) and include mutants for *Nosip*,

Bmp2, *Grm1*, *Bmp2*; *Bmp7* transheterozygote, *Bmp7*, *Ghrhr*, *Fgf10*, and *Papps2*. The processes most strongly correlated to these mutants are histone methylation, dendrite morphogenesis, chromosome segmentation, vasodilation, and fibroblast growth factor binding.

There are a set of mutant phenotypes that have generally low correlations to the set of processes chosen. These mutants include *Fgf3*, *Shh*, *Nipbl*, *Disp*, *Pten*, *Hhat*, and *Alk2*; *Alk3* transheterozygote. Interestingly, this group of mutants vary more along PC2 than PC1 (Figure 8A). Notably, regulation of intracellular protein transport and regulation of cell death are strongly uncorrelated with the majority of mutant directions.

Real-time process GP mapping

Finally, we provide an online tool to visualize process effects and make comparisons to mutant effects in real time. This application is found at genopheno.ucalgary.ca/MGP and can be used for analyses similar to those described in this paper. When the user selects gene ontology terms, the program searches for genotype markers adjacent to each gene listed and uses the selected markers to fit a regularized PLS model. The result is an estimate of the many-to-many relationship between the selected markers and cranial shape variation. The visual outputs include barplots depicting the relative allele effect sizes for each gene in the process and a 3D plot of the corresponding axis of shape variation. Users can compare the effects of different processes and also compare process effects to mutant effects from a provided database of 30 mutant genotypes.

To illustrate how to use this application, we have provided the graphical user interface used to select the parameters (Figure 9). As an example, in the “Process text” entry field, supply a starting term; we chose “brain.” The GO database is then filtered, returning a user-selectable subset of biological process ontology annotation terms in the “Process filter” field. We chose “forebrain morphogenesis,” which has 11 associated genes. We chose to magnify the process phenotype vectors 4x and compare the effect to a heterozygous *Ift88* mutant. *Ift88* is a core component of the primary cilia, which are responsible for promoting developmental signals involved in many facets of facial development (Tian et al., 2017). Further, the plots that are generated are interactive. For example, marker loadings can be highlighted and subset by genes

of interest (Plotly, 2015). There is further information about using this online tool in the “About this app” tab.

Discussion and Conclusion

A key goal in genomics is to create tractable genetic explanations for phenotypic variation. In this study, we used the process MGP approach to model the joint effects of genomic markers on multivariate craniofacial shape. This approach allows us to address the joint contributions of multiple genes that share ontological characteristic such as pathway membership on craniofacial shape as a multivariate trait. Specifically, we chose markers adjacent to genes annotated under a developmental process of interest. We showed three process MGP analyses in depth, each with distinct phenotypic effects. Each of these comparisons highlighted the integrated structure of phenotypic variation in mouse craniofacial shape. We found that while there are processes with distinct and localized effects, genetic effects generally converge on a limited set of directions in phenotype space. Further, these process effects often correspond with the directions of major mutations known to affect these same processes.

Many recent studies have addressed the genetics of craniofacial shape in humans and mice (reviewed in: Roosenboom et al., 2016; Weinberg et al., 2018; White et al. 2021). While these studies are yielding a growing list of genes, suggesting that facial shape is highly polygenic, they have left the vast majority of heritable variation unexplained. Existing studies have either used univariate measures of facial shape such as linear measurements or univariate summaries of multivariate shape (eg. Procrustes distances or PC scores). In addition, most genomic studies of craniofacial shape quantify the effects of each genomic marker independently, with notable exceptions focusing on epistatic effects (eg. Varón-González et al., 2019). Our approach shares common features with some predecessor GP mapping strategies in which candidate genes/SNPs are selected a priori because of common involvement in a pathway (or other mechanistic cluster) (Claes et al., 2014; Liu et al., 2012; Wang et al., 2010, 2007). Wang and colleagues selected SNPs based on proximity to genes of interest and effect size to jointly model the pathway-level effects on Parkinson disease data. Their approach is similar to gene-set enrichment analysis, weighing over-representation of statistical effects related to case-control group membership. In

contrast, our approach focuses on estimating a multivariate set of continuous craniofacial responses. Importantly, our approach jointly identifies genotype-phenotype axes that maximally covary. This differs significantly from approaches that determine phenotypes for analysis *a priori* or based on a pre-determined method of data reduction such as PCA. Our implementation also differs from similar methods like canonical correlation analysis (CCA) that was used to associate single locus effects with a multivariate phenotype (Claes et al., 2018). In comparison with the Process MGP approach, CCA has the advantage of allowing for a parametric hypothesis test, whereas Partial Least Squares analyses are limited to permutation-based hypothesis testing. A distinguishing feature of the Process MGP approach is the ability to penalize the model with regularization. This is ideal for models with many simultaneous genetic effects in order to mitigate the effects of overfitting. Regularization is not unique to PLS, as applications of ridge penalties to CCA have been used for genomic analyses (Waaijenborg & Zwinderman, 2009; Le Floch et al., 2012).

A key finding of our application of the MGP method to craniofacial shape is that multivariate phenotypic variation aligns nonrandomly to genetic markers associated with pathways or developmental processes. Process MGP effects are generally not driven by single loci of large effect are possible, like with the chondrocyte MGP analysis (Figure 2-5A, Figure 6—Supplemental figure 1). These covarying effects represent the joint genetic effects of multiple contributors to phenotypic variance. While these patterns of multivariate genotype-phenotype covariation may include genetic variants that do not actually affect the phenotype, many others will be contributors that we lack statistical power to detect under a typical univariate approach (Pitchers et al., 2019; Varón-González et al., 2019). Here, the overall pattern of genotype-phenotype covariance is the level of genetic explanation for phenotypic variation. When such patterns involve genes that are ontologically linked in meaningful ways, they can provide novel insights into the coordination of genetic effects on phenotypic variation and bolster existing hypotheses from developmental studies.

Another valuable asset that arises from the process MGP approach is the ability to generate testable hypotheses or predictions from multivariate genotype-phenotype observations. The chondrocyte differentiation MGP analysis suggested differentiation defects in the *Bmpr1b*

mutant that could contribute to craniofacial variation. We followed up the MGP analysis with histological analysis of *Bmpr1b* mutants and showed premature suture fusion as well as atypical distribution of hypertrophic chondrocytes in the intersphenoid synchondrosis. Similarly, the analysis of left/right symmetry genes suggested that *Fgf10* alleles can contribute to directional asymmetry. A follow up morphometric analysis of symmetry showed that *Fgf10* mutants do display significant craniofacial asymmetry (Figure 4D). Process MGP can also be used to test existing hypotheses about genotype-phenotype relationships. The relative importance of the *Ankrd11* locus in the palate development analysis and the similarity between the genomic and mutant phenotype further validates the role of *Ankrd11* in palate development. These examples illustrate the additional insights that a process MGP analysis of a mutational effect can provide. Given that such comparisons can be run quickly with our web application, this creates a tool with the potential for hypothesis generation and initial screening for hypotheses about process-level effects on craniofacial variation in mice.

The explicit modeling of multivariate relationships between phenotypes and genotypes also allows a focus on pleiotropy. Developmental studies in mice demonstrate widespread craniofacial morphological effects from localized developmental perturbations (Martínez-Abadías et al., 2012; Stelzer et al., 2007; Young et al., 2010). Perturbations to specific processes in development generally produce effects on multiple aspects of phenotype due to knock-on effects at later stages or to interactions at the level of tissues or anatomical structures (Hallgrímsson et al, 2007). A change in cartilage growth in basicranial synchondroses produces a global change in craniofacial form, for example (Parsons et al, 2015). Remarkably, enhancers with highly specific temporospatial effects on gene expression also produce global rather than localized changes in craniofacial shape (Attanasio et al., 2013). Given that pleiotropy is likely ubiquitous (Hill and Zhang, 2012; Wagner et al, 2008), explicitly multivariate approaches to understanding genotype-phenotype maps are clearly needed.

This convergence of genetic effects on axes of covariation is reflected in our finding that mutations to major developmental genes produce effects that tend to align with the directions of effect associated with the corresponding broader pathways or ontological groups. These results suggest that perturbations that are developmentally similar tend to move the phenotype in the

same direction in multivariate space (Figure 8). Even so, both mutational and higher-level pathway/process effects tend to converge on a few directions of variation suggesting that multiple pathways and processes lead to common developmental outcomes. This conclusion is further supported by our finding that the genetic axes of covariance for individual processes/pathways can align with multiple directions of mutational effect. For example, the process MGP phenotypes clustered in the bottom right of figure 8B are all highly correlated with a set of BMP and growth hormone-related mutants.

In some cases, mutants and MGP map directions do not correspond. There are several ways this can occur. The first is that the DO population may simply lack alleles as deleterious as found in mutant lines. A small effect allele in the DO may not align with the direction of a mutant almost completely lacking expression of the target gene. Further, there are many examples where a mutation may have different and sometimes even opposite effects depending on genetic background (Mackay, 2014; Percival et al., 2017). Mutations of major effect may also differ in direction from variants in related genes that have smaller phenotypic effects due to underlying nonlinearities in development (Green et al., 2017). Investigating how variants in genes that are functionally related vary in phenotypic effect is an important avenue of inquiry that is revealed by analyses such as those we have performed here. Additionally, relationships between process and mutant effects may stimulate hypotheses about previously unknown or unvalidated interactions between loci or pathways.

A second potential reason that MGP effects may not correspond to major mutation effects is the use of only one PLS axis for each process analysis. With only one axis, we only show the phenotypic direction with greatest covariance with genetic marker variation. If there are multiple large marker effects that do not covary, the weaker marker effect will be masked in the analysis. For instance, there may be a PLS axis for “chondrocyte differentiation” that corresponds more strongly with the *Bmp2* mutant phenotype. This phenomenon may be particularly prominent for pathways with substantially different mutant effects, like FGF (Figure 8A). While we did not delve into the directions outside of the first PLS axis, we have facilitated the selection of lower axes in the web application for users to explore and compare with mutants of interest.

Finally, our analysis shares the limitation of all approaches based on gene annotation data. Incomplete annotation may contribute to lead to faulty or incomplete groupings of genes when defining pathway/process hypotheses. Gene annotation is a huge undertaking, and there is substantial variation in the completeness of different process annotations. Many process annotations are manually assigned using inference from the literature, while most are a combination of automated efforts based on transcript similarity and human curation (Mudge and Harrow, 2015). Related to this, we assign gene annotation data to genetic markers based on the closest protein-coding region. While this is a reasonable proxy, there will be regulatory sites that affect genes other than the one immediately adjacent and this is a potential source of uncertainty in our analysis.

In addition, this approach does not currently model the temporal and spatial aspects of gene function throughout development. As a result, alleles of high importance in an MGP analysis don't necessarily produce craniofacial variation through the selected process. A strong allelic effect like *Ccn3* can load heavily in several processes, like "chondrocyte differentiation", "fibroblast migration", and "negative regulation of inflammatory response". We do not know the mechanism through which any individual allele contributes to variation from an MGP analysis alone. Genomic data with more fine grain measurements of variation in expression and utility of individual loci may be better suited to teasing out the potential mechanisms that alleles produce variation.

The MGP method represents a deliberate decision to trade higher level insight from genotype-phenotype association data at the expense of statistical certainty about the significance of individual gene effects. The current implementation of the method also does not allow for quantification of individual epistatic effects. Epistasis occurs when the genotypic trait value for a locus is altered by the genotype of a different locus. Such effects generate nonlinear genotype phenotype maps, but when considered genome-wide, contribute mainly to additive variance (Cheverud and Routman, 1995; Hill, 2017). The MGP method is additive in that it models only the linear effects of genes. However, since it captures the covariances among genotypic effects, much of this "additive" variation is likely epistatic in origin.

Complex traits present a massive challenge in genomics because so many are turning out to be enormously polygenic. To generate tractable explanations of the genetic basis for such traits, methods are needed that extract higher-level representation of genotype-phenotype relationships than those that emerge from single-locus focused approaches. Here, we present a process-driven framework for deriving such higher-level genetic explanations for phenotypic variation. Our approach leverages the biological tendency for developmental processes to produce covariation among aspects of a multivariate phenotypic trait (Hallgrimsson et al., 2009; Wagner et al., 2007). The underlying assumption in this approach is that there are latent variables within high-dimensional genotype-phenotype data that correspond to developmental architecture. We believe that analyses aimed at defining and characterizing such latent variables represent a level of genetic explanation for phenotypic variation that is complementary to genetic analyses designed to establish the significance of single locus effects. Pursuing such questions will help bridge the gap between emerging mechanistic accounts of morphogenesis and our growing understanding of the genetics of morphological variation.

Methods

Mice

We use a sample ($n = 1,145$) of Diversity Outbred mice (DO; Jackson Laboratory, Bar Harbor, ME) to map GP relationships for craniofacial shape (Churchill et al., 2012, 2004). The DO is a multiparental outcross population derived from the eight founding lines of the Collaborative Cross (CC). Each animal's genome is a unique mosaic of the genetic diversity found in the CC—more than 45 million segregating SNPs (CC Consortium, 2012). Random outcrossing over many DO generations maintains this diversity and, with recombination, increases mapping resolution. Discussions of recommended sample sizes in univariate DO studies can be found in Churchill and Gatti (2012; 2014). Both studies recommend a sample size greater than 800 mice for small univariate effect sizes (1-5% variance explained). Further, there are inherent power advantages to our approach because multivariate responses represent maximized differences in phenotype given a set of genotypic measurements. In contrast, univariate approaches such as analyses of

individual principal components can only detect effects along those predefined axes that may not have clear biological significance.

Our DO sample was sourced from three separate laboratories and seven DO generations. 386 are from the Jackson Laboratory (JAX), 287 from the University of North Carolina (UNC), and 472 come from the Scripps Research Institute. Figure 10—figure supplement 1 shows the distribution of the sample by lab source and generation of breeding. Imaging of mice at the University of Calgary was performed under IACUC protocol AC13-0268. Ankrd11 and Bmpr1b mutant mice were bred at the University of Alberta by the Graf lab under Animal Use and Care Committee protocol AUP1149, in accordance with guidelines of the Canadian Council of Animal Care.

Genotyping

Genotyping was performed by Neogen (Lincoln, NE). Ear clippings were used to extract DNA for all samples. Mice from generations 9, 10, and 15 were genotyped using the MegaMUGA genotyping array (77,808 markers); mice from generations 19, 21, 23, and 27 were genotyped using the larger GigaMUGA array (143,259 markers) (Morgan et al., 2016). To pool the genotype data from these two SNP arrays with differing numbers of markers, we imputed markers between the two genotyping arrays using the “calc_genoprob” function in the qtl2 package (Broman et al., 2018). The function uses a hidden Markov model to estimate genotype probabilities and missing genotype data (Gatti et al., 2014). After imputation, the merged genetic dataset consists of 123,309 SNPs which vary among CC founders. Each animal’s genetic record is a 123,309*8 matrix of estimated diplotype contributions of each CC founder to each marker.

Scanning and landmarking

We used micro-computed tomography to acquire 3D scans of the full heads of the mice. Scanning was done at the University of Calgary at .035 mm voxel resolution (Scanco vivaCT40). One of us (WL) then acquired 54 3D landmarks (Figure 10) manually on each volume using Analyze 3D. A discussion of the error associated with manual landmarking can be found in

Percival et al (2019). In addition to the DO phenotype data, the mutant mouse data used for comparisons were collected, scanned, and landmarked between the Hallgrimsson and Marcucio labs.

Landmark registration and analysis

We symmetrized landmarks along the midline of the skull using Klingenberg et al.'s method for object symmetry which configures landmark pairs into a common orientation with reflection and subsequently removes variation associated with translation, scale, and rotation, using Generalized Procrustes Analysis (Adams and Otárola-Castillo, 2013; Klingenberg et al., 2002; Mardia, 2000; Schlager, 2017). We tested for directional asymmetry using the Procrustes ANOVA approach described in Klingenberg et al. (2002). To focus on shared, within-generation patterns in our multigenerational DO sample without sex effects, we regressed symmetric shape on DO generation and sex, and used the residual shapes with the grand mean added as the observations for analysis.

Genetic relatedness

Adjustment of phenotypes for the influence of genetic relatedness is a common approach in genomic studies to prevent spurious associations. However, it is not necessary in all cases, such as situations with low genetic relatedness and little variation in relatedness. We evaluated whether accounting for genetic relatedness was important for our sample. To do so, we estimated a kinship matrix based on DO genotype correlations (Cheng et al., 2013; Broman et al., 2019). The kinship values in our sample have a mean of 0 and a standard deviation of .047. As a result of these findings, we performed all subsequent analyses on the within-generation symmetric shape data, without an adjustment for relatedness.

Regularized PLS analysis

Multivariate genotype-phenotype methods for explicitly modeling multivariate phenotypes and for overcoming the limitations of simple linear regression are increasingly common in mapping

studies. One example of a multivariate genomic approach is found in Claes et al. (2018), where the authors used canonical correlation analysis (CCA) to quantify individual SNP effects for a multivariate measurement of facial shape. CCA returns a vector of the linear combination of phenotypic effects that maximally correlates to the alleles at a given locus. Mitteroecker et al. (2016) developed a similar multivariate strategy around a singular value decomposition (SVD) of genotype-phenotype covariance matrices (versus decomposition of correlation matrices in CCA). Partial least squares (PLS) describes a family of approaches that use SVD to decompose cross covariance matrices (Lee et al., 2011; Mitteroecker and Gunz, 2009; Singh et al., 2016). PLS is increasingly used with large genetic datasets in order to model how genomic effects extend to multiple traits (BJØRNSTAD et al., 2004; Mehmood et al., 2011; Tyler et al., 2017). However, its implementation for MGP mapping is, thus far, much more limited.

SVD decomposes the covariance matrix into three matrices:

$$\mathbf{Y} = \mathbf{U}\mathbf{D}\mathbf{V}'$$

Where \mathbf{Y} is the mean-centered covariance matrix, \mathbf{U} denotes the left singular vectors, a set of vectors of unit length describing the relative weighting of each variable on each axis, and \mathbf{D} denotes the variance along each axis. \mathbf{V} denotes the set of right singular vectors. For a full (square, symmetric) covariance matrix, \mathbf{U} and \mathbf{V} are identical, and the decomposition is equivalent to PCA. For a non-symmetric matrix of covariances, i.e., one describing covariance between two distinct blocks of traits, each successive column of \mathbf{U} and \mathbf{V} provide a pair of singular vectors describing the best least squares approximation of covariance between the two blocks, in order of greatest covariance explained to least.

PLS is most often used to find low-rank linear combinations that maximize covariance between two sets of features. Here, we use the data-driven regularized PLS model implemented in the mddsPLS package to find paired axes that maximize covariance between allelic and shape variation (Lorenzo et al., 2019). The model uses a lasso penalty to minimize the coefficients (loadings) towards zero to prevent overfitting (James et al., 2013). Overfitting can occur in when many genotypic markers are included in the model, particularly when markers are colinear. The

genotype block is composed of the full set of DO founder probabilities for each selected marker. Thus, an analysis of 20 markers would estimate 160 genotype coefficients. The phenotype block consists of the full set of 54 3-dimensional landmarks (162 phenotype coefficients). In all biological process analyses undertaken herein, we used a regularization parameter of 0.06 and report only the first paired axes of the PLS model, i.e., the genotype and phenotype axes which explain the most covariance.

We generate graphical displays of process results using the R packages `ggplot2` (Wickham, 2016) and `Morpho` (Schlager, 2017). An example script to reproduce the analyses is provided at github.com/j0vid/MGP_shiny/analyses.

Statistical results and comparisons

We estimate the magnitude and direction of MGP process effects using R^2 and vector correlations, respectively. R^2 is calculated as the ratio of trace of the predicted model covariance to the trace of the phenotypic covariance matrix. We contextualize the MGP process R^2 by comparing it to the R^2 value of 10000 randomly drawn marker sets of the same size. For instance, a process annotated with 40 genes would be compared to 10000 40-gene MGP analyses with random markers selected in each iteration. Random marker selection for permutation is constrained to follow similar patterns of linkage disequilibrium to the observed marker set of interest. The null expectation in this scenario is that gene annotation does not provide better information about coordinated marker effects than a randomly selected set of markers.

Vector correlations between process MGP effects are calculated by taking the Pearson product-moment correlation of the two sets of process PLS1 phenotypic loadings. Vector correlations between process effects and mutant effects are calculated by taking the correlation between the process PLS1 phenotypic loadings and mutant MANOVA coefficients. The MANOVA was used to compare the mutant group phenotype against the DO sample specified as the reference group. The coefficients of the MANOVA describe the relative weights of each landmark coordinate difference between the DO mean shape and the mutant mean shape.

Chondrocyte morphometrics

Chondrocyte morphometrics were performed using a novel technique developed by the Marcucio laboratory. Images of the intersphenoid synchondrosis (ISS) were stained with H&E, SafO, or picrosirius red were captured and imported into ImageJ (2-6 sections from at least 4 mice/genotype/synchondrosis). Landmarks were placed in a defined order (left, right, top, bottom) of visible chondrocytes in the synchondrosis using the ImageJ's multi-tool. Data points were then exported as XY coordinates and imported into Microsoft Excel for calculation of major and minor axes relative to overall width of synchondrosis. Area of individual cells was determined from height and width values based on assumption that each cell is roughly ellipsoidal. An example of major and minor axis measurements and ellipsoidal area measurements on a slide is provided in Figure 3—figure supplement 1.

We compared differences in the distribution of cell sizes along normalized synchondroses between *Bmpr1b* mutants and controls with a mixed effects model approach. We used ellipsoidal area of cell size (in microns) as our dependent variable. For fixed effects, we modelled the normalized synchondrosis position (1st and 2nd order), where a value of 0 represents the relative midline of the synchondrosis and values of -1 and 1 represent the most distant cells in that synchondrosis. We also modelled genotype as a fixed effect as well as a genotype by cell position interaction (both 1st and 2nd order interactions). For each individual within each genotype, we measured multiple histological sections. These repeated and nested measurements of cell size in multiple sections for each individual were modelled as random effects. To test for cell size differences between genotypes, we used a likelihood ratio test to compare the full model to a reduced model with the fixed effect of genotype and all genotype interactions removed.

Visualization tools

We introduce an interactive web application that allows the user to select processes of interest with a graphical user interface and see the resulting craniofacial effect at genopheno.ucalgary.ca/MGP. The web apps were written using the shiny package in R (Chang et al., 2018). The application dynamically filters the MGI GO database based on the initial user

input. Queries will only list GO terms with exact matches. For example, “chond” will return GO terms that incorporate either “chondrocyte” and “mitochondria”.

Multiple queries can be selected. An analysis of “chondrocyte differentiation” and “chondrocyte hypertrophy” will select the joint gene set of both processes. Processes with different names can be jointly queried with the pipe operator “|”, which is interpreted as an OR (union) operator. For example, to generate the list of GO terms associated with either apoptosis or WNT, we used the “apoptosis|WNT” query and selected the processes “Wnt signaling pathway” and “execution phase of apoptosis” to perform the analysis on the joint set of associated genes (Figure 9—figure supplement 1).

Several other parameters can be specified by the user including the type of plot to be generated for the genetic loadings, the amount of magnification applied to the phenotype effect vectors, the regularization parameter, and the option to overlay a mutant phenotype for comparison. The comparative database currently includes craniofacial shape contrast data (wild-type vs. mutant) for 30 mutant genotypes. If a mutant comparison is selected, the full set of DO specimens are registered with the mutants added (with size removed). We then provide the vector correlation between the process effect and the mutant effect (see Figure 9). The database also includes PC1 of the DO sample for comparison.

The app enables users to save results. A save request will generate and download an HTML report of the analysis which includes several versions of the genetic effect plot and an interactive 3D model of the estimated phenotypic effect. If a mutant comparison is selected, it will also appear in the report.

The application tracks recent searches by the user for their reference. A heatmap of process vector correlations of the PLS phenotype loadings is also available under the “recent searches” tab. The user can select between a heatmap of the processes in their search history or a random assortment of process correlations from past, anonymous user searches.

Finally, we provide programmatic access to our model for both process MGP analyses as well as custom gene lists over the web through an application programming interface (API). Queries can be formatted using curl commands as well request URLs and return results in JavaScript object notation (JSON) format. Documentation for the available functions and their parameters, as well as examples for queries can be found at genopheno.ucalgary.ca/api/___docs___/. The API was written using the plumber package (Schloerke & Allen, 2021) in R, with code available at github.com/j0vid/MGP_shiny/MGP_API.

Acknowledgements:

Grants: NIH - 2R01DE019638 to RM, BH and JC, NSERC 238992-17, CIHR Foundation grant 159920 to BH, CFI grant #36262 to BH and NSERC RGPIN-2014-06311 to DG. JDA is supported by an Eyes High fellowship, an Alberta Children's Hospital Research Institute scholarship and a MITACS graduate fellowship.

References

- Albertson RC, Yelick PC. 2005. Roles for fgf8 signaling in left–right patterning of the visceral organs and craniofacial skeleton. *Developmental Biology* **283**:2. doi:10.1016/j.ydbio.2005.04.025
- Attanasio C, Nord AS, Zhu Y, Blow MJ, Li Z, Liberton DK, Morrison H, Plajzer-Frick I, Holt A, Hosseini R, Phouanavong S, Akiyama JA, Shoukry M, Afzal V, Rubin EM, FitzPatrick DR, Ren B, Hallgrímsson B, Pennacchio LA, Visel A. 2013. Fine Tuning of Craniofacial Morphology by Distant-Acting Enhancers. *Science* **342**:1241006. doi:10.1126/science.1241006
- Brazil DP, Church RH, Surae S, Godson C, Martin F. 2015. BMP signalling: agony and antagonism in the family. *Trends Cell Biol* **25**:249–264. doi:10.1016/j.tcb.2014.12.004
- Broman K, Sen S. (2009). A Guide to QTL Mapping with R/qtl. Springer. ISBN 978-0-387-92125-9. <https://doi.org/10.1007/978-0-387-92125-9>
- Broman K, Gatti D, Simecek P, Furlotte N, Prins P, Sen S, Yandell B, Churchill G. (2018). R/qtl2: Software for Mapping Quantitative Trait Loci with High-Dimensional Data and Multi-parent Populations Genetics 211(2), genetics.301595.2018. <https://dx.doi.org/10.1534/genetics.118.301595>
- Chai Y. 2015. Craniofacial Development. *Current Topics in Dev Bio*. Academic Press. Volume 115. ISBN 9780124081413.
- Chebib J, Guillaume F. 2017. What affects the predictability of evolutionary constraints using a G-matrix? The relative effects of modular pleiotropy and mutational correlation. *Evol Int J Org Evol* **71**:2298–2312. doi:10.1111/evo.13320
- Cheverud JM, Routman EJ. 1996. EPISTASIS AS A SOURCE OF INCREASED ADDITIVE GENETIC VARIANCE AT POPULATION BOTTLENECKS. *Evolution* **50**:1042–1051. doi:10.1111/j.1558-5646.1996.tb02345.x
- Churchill GA, Gatti DM, Munger SC, Svenson KL. 2012. The diversity outbred mouse population. *Mamm Genome* **23**:713–718. doi:10.1007/s00335-012-9414-2
- Claes P, Liberton DK, Daniels K, Rosana KM, Quillen EE, Pearson LN, McEvoy B, Bauchet M, Zaidi AA, Yao W, Tang H, Barsh GS, Absher DM, Puts DA, Rocha J, Beleza S, Pereira RW, Baynam G, Suetens P, Vandermeulen D, Wagner JK, Boster JS, Shriver MD. 2014. Modeling 3D Facial Shape from DNA. *Plos Genet* **10**:e1004224. doi:10.1371/journal.pgen.1004224
- Claes P, Roosenboom J, White J. D., Swigut T, Sero D, Li J, Lee M. K., Zaidi A., Mattern B. C., Liebowitz C., Pearson L., González T., Leslie E. J., Carlson J. C., Orlova E., Suetens P., Vandermeulen D., Feingold E., Marazita M. L., Shaffer J. R., Wysocka J., Shriver M. D., & Weinberg S. M. (2018). Genome-wide mapping of global-to-local genetic effects on human facial shape. *Nature Genetics*, **50**(3), 414–423. doi:10.1038/s41588-018-0057-4

852 Cole, J. B., Manyama, M., Kimwaga, E., Mathayo, J., Larson, J. R., Liberton, D. K., Lukowiak,
853 K., Ferrara, T. M., Riccardi, S. L., Li, M., Mio, W., Prochazkova, M., Williams, T., Li, H.,
854 Jones, K. L., Klein, O. D., Santorico, S. A., Hallgrimsson, B., & Spritz, R. A. (2016).
855 Genomewide Association Study of African Children Identifies Association of SCHIP1 and
856 PDE8A with Facial Size and Shape. *PLoS Genetics*, **12**(8), e1006174.
857 doi:10.1371/journal.pgen.1006174

858 Cole JB, Manyama M, Larson JR, Liberton DK, Ferrara TM, Riccardi SL, Li M, Mio W, Klein
859 OD, Santorico SA, Hallgrímsson B, Spritz RA. 2017. Human Facial Shape and Size
860 Heritability and Genetic Correlations. *Genetics* **205**:967–978.
861 doi:10.1534/genetics.116.193185

862 Collaborative Cross Consortium. 2012. The Genome Architecture of the Collaborative Cross
863 Mouse Genetic Reference Population. *Genetics* **190**:389–401.
864 doi:10.1534/genetics.111.132639

865 Dudbridge F. 2013. Power and Predictive Accuracy of Polygenic Risk Scores. *Plos Genet*
866 **9**:e1003348. doi:10.1371/journal.pgen.1003348

867 FANTOM Consortium, Forrest ARR, Kawaji H, Rehli M, Baillie JK, Hoon MJL de, Haberle V,
868 Lassmann T, Kulakovskiy IV, Lizio M, Itoh M, Andersson R, Mungall CJ, Meehan TF,
869 Schmeier S, Bertin N, Jørgensen M, Dimont E, Arner E, Schmidl C, Schaefer U, Medvedeva
870 YA, Plessy C, Vitezic M, Severin J, Semple CA, Ishizu Y, Young RS, Francescato M, Alam
871 I, Albanese D, Altschuler GM, Arakawa T, Archer JAC, Arner P, Babina M, Rennie S,
872 Balwierz PJ, Beckhouse AG, Pradhan-Bhatt S, Blake JA, Blumenthal A, Bodega B, Bonetti A,
873 Briggs J, Brombacher F, Burroughs AM, Califano A, Cannistraci CV, Carbajo D, Chen Y,
874 Chierici M, Ciani Y, Clevers HC, Dalla E, Davis CA, Detmar M, Diehl AD, Dohi T, Drabløs
875 F, Edge ASB, Edinger M, Ekwall K, Endoh M, Enomoto H, Fagiolini M, Fairbairn L, Fang H,
876 Farach-Carson MC, Faulkner GJ, Favorov AV, Fisher ME, Frith MC, Fujita R, Fukuda S,
877 Furlanello C, Furuno M, Furusawa J, Geijtenbeek TB, Gibson AP, Gingeras T, Goldowitz D,
878 Gough J, Guhl S, Guler R, Gustincich S, Ha TJ, Hamaguchi M, Hara M, Harbers M,
879 Harshbarger J, Hasegawa A, Hasegawa Y, Hashimoto T, Herlyn M, Hitchens KJ, Sui SJH,
880 Hofmann OM, Hoof I, Hori F, Huminiecki L, Iida K, Ikawa T, Jankovic BR, Jia H, Joshi A,
881 Jurman G, Kaczowski B, Kai C, Kaida K, Kaiho A, Kajiyama K, Kanamori-Katayama M,
882 Kasianov AS, Kasukawa T, Katayama S, Kato S, Kawaguchi S, Kawamoto H, Kawamura YI,
883 Kawashima T, Kempfle JS, Kenna TJ, Kere J, Khachigian LM, Kitamura T, Klinken SP,
884 Knox AJ, Kojima M, Kojima S, Kondo N, Koseki H, Koyasu S, Krampitz S, Kubosaki A,
885 Kwon AT, Laros JFJ, Lee W, Lennartsson A, Li K, Lilje B, Lipovich L, Mackay-sim A,
886 Manabe R, Mar JC, Marchand B, Mathelier A, Meijert N, Meynert A, Mizuno Y, Morais DA
887 de L, Morikawa H, Morimoto M, Moro K, Motakis E, Motohashi H, Mummery CL, Murata
888 M, Nagao-Sato S, Nakachi Y, Nakahara F, Nakamura T, Nakamura Y, Nakazato K,
889 Nimwegen E van, Ninomiya N, Nishiyori H, Noma S, Nozaki T, Ogishima S, Ohkura N,
890 Ohmiya H, Ohno H, Ohshima M, Okada-Hatakeyama M, Okazaki Y, Orlando V,
891 Ovchinnikov DA, Pain A, Passier R, Patrikakis M, Persson H, Piazza S, Prendergast JGD,
892 Rackham OJL, Ramilowski JA, Rashid M, Ravasi T, Rizzu P, Roncador M, Roy S, Rye MB,
893 Saijyo E, Sajantila A, Saka A, Sakaguchi S, Sakai M, Sato H, Satoh H, Savvi S, Saxena A,

894 Schneider C, Schultes EA, Schulze-Tanzil GG, Schwegmann A, Sengstag T, Sheng G,
895 Shimoji H, Shimoni Y, Shin JW, Simon C, Sugiyama D, Sugiyama T, Suzuki M, Suzuki N,
896 Swoboda RK, Hoen PAC 't, Tagami M, Takahashi N, Takai J, Tanaka H, Tatsukawa H,
897 Tatum Z, Thompson M, Toyoda H, Toyoda T, Valen E, Wetering M van de, Berg LM van
898 den, Verardo R, Vijayan D, Vorontsov IE, Wasserman WW, Watanabe S, Wells CA,
899 Winteringham LN, Wolvetang E, Wood EJ, Yamaguchi Y, Yamamoto M, Yoneda M,
900 Yonekura Y, Yoshida S, Zabierowski SE, Zhang PG, Zhao X, Zucchelli S, Summers KM,
901 Suzuki H, Daub CO, Kawai J, Heutink P, Hide W, Freeman TC, Lenhard B, Bajic VB, Taylor
902 MS, Makeev VJ, Sandelin A, Hume DA, Carninci P, Hayashizaki Y. 2014. A promoter-level
903 mammalian expression atlas. *Nature* **507**:462. doi:10.1038/nature13182

904 Finger JH, Smith CM, Hayamizu TF, McCright IJ, Xu J, Law M, Shaw DR, Baldarelli RM, Beal
905 JS, Blodgett O, Campbell JW, Corbani LE, Lewis JR, Forthofer KL, Frost PJ, Giannatto SC,
906 Hutchins LN, Miers DB, Motenko H, Stone KR, Eppig JT, Kadin JA, Richardson JE,
907 Ringwald M. 2017. The mouse Gene Expression Database (GXD): 2017 update. *Nucleic
908 Acids Res* **45**:D730–D736. doi:10.1093/nar/gkw1073

909 Francis-West P, Crespo-Enriquez I. 2016. Vertebrate Embryo: Craniofacial Development. *eLS*
910 1–15. doi:10.1002/9780470015902.a0026602

911 Gasch AP, Payseur BA, Pool JE. 2016. The Power of Natural Variation for Model Organism
912 Biology. *Trends Genet* **32**:147–154. doi:10.1016/j.tig.2015.12.003

913 Gatti DM, Svenson KL, Shabalin A, Wu L-Y, Valdar W, Simecek P, Goodwin N, Cheng R,
914 Pomp D, Palmer A, Chesler EJ, Broman KW, Churchill GA. 2014. Quantitative Trait Locus
915 Mapping Methods for Diversity Outbred Mice. *G3 Genes Genomes Genetics* **4**:1623–1633.
916 doi:10.1534/g3.114.013748

917 Gonzalez, PN, Kristensen, E, Morck, DW, Boyd, S, Hallgrímsson, B. 2013. Effects of growth
918 hormone on the ontogenetic allometry of craniofacial bones. *Evolution & Development* **15**:
919 133-145. doi:[10.1111/ede.12025](https://doi.org/10.1111/ede.12025)

920 Green RM, Fish JL, Young NM, Smith FJ, Roberts B, Dolan K, Choi I, Leach CL, Gordon P,
921 Cheverud JM, Roseman CC, Williams TJ, Marcucio RS, Hallgrímsson B. 2017.
922 Developmental nonlinearity drives phenotypic robustness. *Nat Commun* **8**:1970.
923 doi:10.1038/s41467-017-02037-7

924 Greene RM, Pisano MM. 2010. Palate morphogenesis: Current understanding and future
925 directions. *Birth Defects Res Part C Embryo Today Rev* **90**:133–154. doi:10.1002/bdrc.20180

926 Hallgrimsson, B, Lieberman, DE, Liu, W, Ford-Hutchinson, AF, Jirik, FR. 2007. Epigenetic
927 interactions and the structure of phenotypic variation in the cranium. *Evol Dev* **9**(1), 76-91.

928 Hallgrimsson B, Green RM, Katz DC, Fish JL, Bernier FP, Roseman CC, Young NM, Cheverud
929 JM, Marcucio RS. 2018. The developmental-genetics of canalization. *Semin Cell Dev Biol*.
930 doi:10.1016/j.semcdb.2018.05.019

931 Hallgrímsson B, Jamniczky H, Young NM, Rolian C, Parsons TE, Boughner JC, Marcucio RS.
 932 2009. Deciphering the Palimpsest: Studying the Relationship Between Morphological
 933 Integration and Phenotypic Covariation. *Evol Biol* **36**:355–376. doi:10.1007/s11692-009-
 934 9076-5

935 Hallgrímsson B, Lieberman DE. 2008. Mouse models and the evolutionary developmental
 936 biology of the skull. *Integr Comp Biol* **48**:373–384. doi:10.1093/icb/icn076

937 Hallgrímsson B, Mio W, Marcucio RS, Spritz R. 2014. Let's Face It—Complex Traits Are Just
 938 Not That Simple. *Plos Genet* **10**:e1004724. doi:10.1371/journal.pgen.1004724

939 Hecksher-Sørensen J, Watson RP, Lettice LA, Serup P, Eley L, De Angelis C, Ahlgren U, Hill
 940 RE. 2004. The splanchnic mesodermal plate directs spleen and pancreatic laterality, and is
 941 regulated by *Bapx1/Nkx3.2*. *Development* **131** (19): 4665–4675. doi:[10.1242/dev.01364](https://doi.org/10.1242/dev.01364)

942 Hilliard SA, Yu L, Gu S, Zhang Z, Chen YP. 2005. Regional regulation of palatal growth and
 943 patterning along the anterior–posterior axis in mice. *J Anat* **207**:655–667. doi:10.1111/j.1469-
 944 7580.2005.00474.x

945 Houle D, Fierst J. 2012. Properties of spontaneous mutational variance and covariance for wing
 946 size and shape in *Drosophila melanogaster*. *Evol Int J Org Evol* **67**:1116–30.
 947 doi:10.1111/j.1558-5646.2012.01838.x

948 Houle D, Govindaraju DR, Omholt S. 2010. Phenomics: the next challenge. *Nat Rev Genet*
 949 **11**:855. doi:10.1038/nrg2897

950 Jin Y-R, Han XH, Taketo MM, Yoon JK. 2012. Wnt9b-dependent FGF signaling is crucial for
 951 outgrowth of the nasal and maxillary processes during upper jaw and lip development.
 952 *Development* **139**:1821–1830. doi:10.1242/dev.075796

953 Johannsdottir B, Thorarinsson F, Thordarson A, Magnusson TE. 2005. Heritability of
 954 craniofacial characteristics between parents and offspring estimated from lateral
 955 cephalograms. *Am J Orthod Dentofac* **127**:200–207. doi:10.1016/j.ajodo.2004.07.033

956 Kanehisa M, Furumichi M, Tanabe M, Sato Y, Morishima K. 2017. KEGG: new perspectives on
 957 genomes, pathways, diseases and drugs. *Nucleic Acids Res* **45**:D353–D361.
 958 doi:10.1093/nar/gkw1092

959 Katz DC, Aponte JD, Liu W, Green RM, Mayeux JM, Pollard KM, Pomp D, Munger SC,
 960 Murray SA, Roseman CC, Percival CJ, Cheverud J, Marcucio RS, Hallgrímsson B. 2019.
 961 Facial shape and allometry quantitative trait locus intervals in the Diversity Outbred mouse
 962 are enriched for known skeletal and facial development genes. *Biorxiv* 787291.
 963 doi:10.1101/787291

964 Kawauchi S, Calof AL, Santos R, Lopez-Burks ME, Young CM, Hoang MP, Chua A, Lao T,
 965 Lechner MS, Daniel JA, Nussenzweig A, Kitzes L, Yokomori K, Hallgrímsson B, Lander AD.

2009. Multiple Organ System Defects and Transcriptional Dysregulation in the *Nipbl*^{+/-} Mouse, a Model of Cornelia de Lange Syndrome. *Plos Genet* **5**:e1000650. doi:10.1371/journal.pgen.1000650

Kenney-Hunt JP, Wang B, Norgard EA, Fawcett G, Falk D, Pletscher LS, Jarvis JP, Roseman C, Wolf J, Cheverud JM. 2008. Pleiotropic Patterns of Quantitative Trait Loci for 70 Murine Skeletal Traits. *Genetics* **178**:2275–2288. doi:10.1534/genetics.107.084434

Klingenberg CP, Leamy LJ. 2001. QUANTITATIVE GENETICS OF GEOMETRIC SHAPE IN THE MOUSE MANDIBLE. *Evolution* **55**:2342–2352. doi:10.1554/0014-3820(2001)055[2342:qgogsi]2.0.co;2

Klingenberg CP, Barluenga M, Meyer A. Shape analysis of symmetric structures: quantifying variation among individuals and asymmetry. *Evolution*. 2002 Oct;56(10):1909-20. doi: 10.1111/j.0014-3820.2002.tb00117.x. PMID: 12449478.

le Floch, D., Guillemot, V., Frouin, V., Pinel, P., Lalanne, C., Trinchera, L., Tenenhaus, A., Moreno, A., Zilbovicius, M., Bourgeron, T., Dehaene, S., Thirion, B., Poline, J. B., & Duchesnay, D. (2012). Significant correlation between a set of genetic polymorphisms and a functional brain network revealed by feature selection and sparse Partial Least Squares. *NeuroImage*, **63**(1), 11–24. <https://doi.org/10.1016/j.neuroimage.2012.06.061>

Lewontin R. 1974. The Genetic Basis of Evolutionary Change. New York, Columbia University Press, 1974.

Liu F, Lijn F van der, Schurmann C, Zhu G, Chakravarty MM, Hysi PG, Wollstein A, Lao O, Bruijne M de, Ikram MA, Lugt A van der, Rivadeneira F, Uitterlinden AG, Hofman A, Niessen WJ, Homuth G, Zubicaray G de, McMahon KL, Thompson PM, Daboul A, Puls R, Hegenscheid K, Bevan L, Pausova Z, Medland SE, Montgomery GW, Wright MJ, Wicking C, Boehringer S, Spector TD, Paus T, Martin NG, Biffar R, Kayser M. 2012. A Genome-Wide Association Study Identifies Five Loci Influencing Facial Morphology in Europeans. *Plos Genet* **8**:e1002932. doi:10.1371/journal.pgen.1002932

Liu W, Sun X, Braut A, Mishina Y, Behringer RR, Mina M, Martin JF. 2005. Distinct functions for Bmp signaling in lip and palate fusion in mice. *Development* **132**:1453–1461. doi:10.1242/dev.01676

Liu X, Hayano S, Pan H, Inagaki M, Ninomiya-Tsuji J, Sun H, Mishina Y. 2018. Compound Mutations in *Bmpr1a* and *Tak1* Synergize Facial Deformities Via Increased Cell Death. *Genesis* **56**(3):e23093. doi: 10.1002/dvg.23093

Lorenzo H, Saracco J, Thiébaud R. 2019. Supervised Learning for Multi-Block Incomplete Data. arXiv preprint *arXiv*:1901.04380. <http://arxiv.org/abs/1901.04380>

Low K, Ashraf T, Canham N, Clayton-Smith J, Deshpande C, Donaldson A, Fisher R, Flinter F, Foulds N, Fryer A, Gibson K, Hayes I, Hills A, Holder S, Irving M, Joss S, Kivuva E,

1002 Lachlan K, Magee A, McConnell V, McEntagart M, Metcalfe K, Montgomery T, Newbury-
1003 Ecob R, Stewart F, Turnpenny P, Vogt J, Fitzpatrick D, Williams M, Study D, Smithson S.
1004 2016. Clinical and genetic aspects of KBG syndrome. *Am J Med Genet A* **170**:2835–2846.
1005 doi:10.1002/ajmg.a.37842

1006 Mackay, T. Epistasis and quantitative traits: using model organisms to study gene–gene
1007 interactions. *Nat Rev Genet* **15**, 22–33 (2014). <https://doi.org/10.1038/nrg3627>

1008 Mackay TF, Moore JH. 2014. Why epistasis is important for tackling complex human disease
1009 genetics. *Genome Med* **6**:42. doi:10.1186/gm561

1010 Maga AM, Navarro N, Cunningham ML, Cox TC. 2015. Quantitative trait loci affecting the 3D
1011 skull shape and size in mouse and prioritization of candidate genes in-silico. *Front Physiol*
1012 **6**:92. doi:10.3389/fphys.2015.00092

1013 Martínez-Abadías N, Mitteroecker P, Parsons TE, Esparza M, Sjøvold T, Rolian C, Richtsmeier
1014 JT, Hallgrímsson B. 2012. The Developmental Basis of Quantitative Craniofacial Variation in
1015 Humans and Mice. *Evol Biol* **39**:554–567. doi:10.1007/s11692-012-9210-7

1016 Mattick JS, Taft RJ, Faulkner GJ. 2010. A global view of genomic information – moving beyond
1017 the gene and the master regulator. *Trends Genet* **26**:21–28. doi:10.1016/j.tig.2009.11.002

1018 Mitteroecker P, Cheverud JM, Pavlicev M. 2016. Multivariate Analysis of Genotype–Phenotype
1019 Association. *Genetics* **202**:1345–1363. doi:10.1534/genetics.115.181339

1020 Morozova TV, Huang W, Pray VA, Whitham T, Anholt RRH, Mackay TFC. 2015.
1021 Polymorphisms in early neurodevelopmental genes affect natural variation in alcohol
1022 sensitivity in adult drosophila. *Bmc Genomics* **16**:865. doi:10.1186/s12864-015-2064-5

1023 Mudge JM, Harrow J. 2015. Creating reference gene annotation for the mouse C57BL6/J
1024 genome assembly. *Mamm Genome* **26**:366–378. doi:10.1007/s00335-015-9583-x

1025 Nakata M. 1985. Twin Studies in Craniofacial Genetics: A Review. *Amg Acta Geneticae*
1026 *Medicae Et Gemellologiae Twin Res* **34**:1–14. doi:10.1017/s0001566000004876

1027 Ornitz DM, Marie PJ. 2015. Fibroblast growth factor signaling in skeletal development and
1028 disease. *Gene Dev* **29**:1463–1486. doi:10.1101/gad.266551.115

1029 Pallares LF, Carbonetto P, Gopalakrishnan S, Parker CC, Ackert-Bicknell CL, Palmer AA, Tautz
1030 D. 2015. Mapping of Craniofacial Traits in Outbred Mice Identifies Major Developmental
1031 Genes Involved in Shape Determination. *Plos Genet* **11**:e1005607.
1032 doi:10.1371/journal.pgen.1005607

1033 Pallares LF, Harr B, Turner LM, Tautz D. 2014. Use of a natural hybrid zone for genomewide
1034 association mapping of craniofacial traits in the house mouse. *Mol Ecol* **23**:5756–5770.
1035 doi:10.1111/mec.12968

- 1036 Parsons, T. E., Downey, C. M., Jirik, F. R., Hallgrímsson, B., & Jamniczky, H. A. (2015). Mind
1037 the Gap: Genetic Manipulation of Basicranial Growth within Synchronoses Modulates
1038 Calvarial and Facial Shape in Mice through Epigenetic Interactions. *PloS One*, *10*(2),
1039 e0118355. doi:10.1371/journal.pone.0118355
- 1040 Percival CJ, Marangoni P, Tapaltsyan V, Klein O, Hallgrímsson B. 2017. The Interaction of
1041 Genetic Background and Mutational Effects in Regulation of Mouse Craniofacial Shape. *G3*
1042 *Genes Genomes Genetics* **7**:1439–1450. doi:10.1534/g3.117.040659
- 1043 Percival CJ, Richtsmeier JT. 2013. Angiogenesis and intramembranous osteogenesis. *Dev*
1044 *Dynam* **242**:909–922. doi:10.1002/dvdy.23992
- 1045 Pitchers W, Nye J, Márquez EJ, Kowalski A, Dworkin I, Houle D. 2019. A Multivariate
1046 Genome-Wide Association Study of Wing Shape in *Drosophila melanogaster*. *Genetics*
1047 **211**:genetics.301342.2018. doi:10.1534/genetics.118.301342
- 1048 Plotly Technologies Inc. Collaborative data science. Montréal, QC, 2015. <https://plot.ly>.
- 1049 Prochazkova M, Prochazka J, Marangoni P, Klein OD. 2018. Bones, Glands, Ears and More:
1050 The Multiple Roles of FGF10 in Craniofacial Development. *Frontiers Genetics* **9**:542.
1051 doi:10.3389/fgene.2018.00542
- 1052 R Core Team (2017). R: A language and environment for statistical computing. R Foundation for
1053 Statistical Computing, Vienna, Austria. URL <https://www.R-project.org/>.
- 1054 Reed LK, Baer CF, Edison AS. 2017. Considerations when choosing a genetic model organism
1055 for metabolomics studies. *Curr Opin Chem Biol* **36**:7–14. doi:10.1016/j.cbpa.2016.12.005
- 1056 Rendel, J. M. (1967). *Canalization and gene control*. London: Logos Press.
- 1057 Richman JM, Herbert M, Matovinovic E, Walin J. 1997. Effect of Fibroblast Growth Factors on
1058 Outgrowth of Facial Mesenchyme. *Dev Biol* **189**:135–147. doi:10.1006/dbio.1997.8656
- 1059 Richtsmeier JT, Flaherty K. 2013. Hand in glove: brain and skull in development and
1060 dysmorphogenesis. *Acta Neuropathol* **125**:469–489. doi:10.1007/s00401-013-1104-y
- 1061 Rie D de, Abugessaisa I, Alam T, Arner E, Arner P, Ashoor H, Åström G, Babina M, Bertin N,
1062 Burroughs AM, Carlisle AJ, Daub CO, Detmar M, Deviatiiarov R, Fort A, Gebhard C,
1063 Goldowitz D, Guhl S, Ha TJ, Harshbarger J, Hasegawa A, Hashimoto K, Herlyn M, Heutink
1064 P, Hitchens KJ, Hon CC, Huang E, Ishizu Y, Kai C, Kasukawa T, Klinken P, Lassmann T,
1065 Lecellier C-H, Lee W, Lizio M, Makeev V, Mathelier A, Medvedeva YA, Mejhert N,
1066 Mungall CJ, Noma S, Ohshima M, Okada-Hatakeyama M, Persson H, Rizzu P, Roudnický F,
1067 Sætrom P, Sato H, Severin J, Shin JW, Swoboda RK, Tarui H, Toyoda H, Vitting-Seerup K,
1068 Winteringham L, Yamaguchi Y, Yasuzawa K, Yoneda M, Yumoto N, Zabierowski S, Zhang
1069 PG, Wells CA, Summers KM, Kawaji H, Sandelin A, Rehli M, Consortium TF, Hayashizaki

1070 Y, Carninci P, Forrest ARR, Hoon MJL de. 2017. An integrated expression atlas of miRNAs
1071 and their promoters in human and mouse. *Nat Biotechnol* **35**:nbt.3947. doi:10.1038/nbt.3947

1072 Roosenboom J, Hens G, Mattern BC, Shriver MD, Claes P. 2016. Exploring the Underlying
1073 Genetics of Craniofacial Morphology through Various Sources of Knowledge. *Biomed Res*
1074 *Int* **2016**:1–9. doi:10.1155/2016/3054578

1075 Rueden CT, Schindelin J, Hiner MC, DeZonia BE, Walter AE, Arena ET, Eliceiri KW. 2017.
1076 ImageJ2: ImageJ for the next generation of scientific image data. *Bmc Bioinformatics* **18**:529.
1077 doi:10.1186/s12859-017-1934-z

1078 Schloerke B, Allen J. 2021. plumber: An API Generator for R. R package version
1079 1.1.0. <https://CRAN.R-project.org/package=plumber>

1080 Shaffer, J. R., Orlova, E., Lee, M. K., Leslie, E. J., Raffensperger, Z. D., Heike, C. L.,
1081 Cunningham, M. L., Hecht, J. T., Kau, C. H., Nidey, N. L., Moreno, L. M., Wehby, G. L.,
1082 Murray, J. C., Laurie, C. A., Laurie, C. C., Cole, J., Ferrara, T., Santorico, S., Klein, O., Mio, W.,
1083 Feingold, E., Hallgrimsson, B., Spritz, R. A., Marazita, M. L., & Weinberg, S. M. 2016.
1084 Genome-Wide Association Study Reveals Multiple Loci Influencing Normal Human Facial
1085 Morphology. *PLoS Genetics*, **12**(8), e1006149. doi:10.1371/journal.pgen.1006149

1086 Schoenfelder S, Javierre B-M, Furlan-Magaril M, Wingett SW, Fraser P. 2018. Promoter
1087 Capture Hi-C: High-resolution, Genome-wide Profiling of Promoter Interactions. *J Vis Exp*
1088 *Jove* 57320. doi:10.3791/57320

1089 Sneath, P.H.A. and Sokal, R.R. 1973 Numerical Taxonomy: The Principles and Practice of
1090 Numerical Classification, p. 279; Freeman, San Francisco.

1091 Sprinzak E, Margalit H. 2001. Correlated sequence-signatures as markers of protein-protein
1092 interaction1 Edited by G. von Heijne. *J Mol Biol* **311**:681–692. doi:10.1006/jmbi.2001.4920

1093 Stelzer C, Brimmer A, Hermanns P, Zabel B, Dietz UH. 2007. Expression profile of Papss2 (3'-
1094 phosphoadenosine 5'-phosphosulfate synthase 2) during cartilage formation and skeletal
1095 development in the mouse embryo. *Dev Dynam* **236**:1313–1318. doi:10.1002/dvdy.21137

1096 Tian H, Feng J, Li J, Ho T-V, Yuan Y, Liu Y, Brindopke F, Figueiredo JC, Magee W, Sanchez-
1097 Lara PA, Chai Y. 2017. Intraflagellar transport 88 (IFT88) is crucial for craniofacial
1098 development in mice and is a candidate gene for human cleft lip and palate. *Hum Mol Genet*
1099 *ddx002*. doi:10.1093/hmg/ddx002

1100 Tsagkraloulis D, Hysi P, Spector T, Montana G. 2017. Heritability maps of human face
1101 morphology through large-scale automated three-dimensional phenotyping. *Sci Rep-uk*
1102 **7**:45885. doi:10.1038/srep45885

- 1103 Uller T, Moczek AP, Watson RA, Brakefield PM, Laland KN. 2018. Developmental Bias and
1104 Evolution: A Regulatory Network Perspective. *Genetics* **209**:949–966.
1105 doi:10.1534/genetics.118.300995
- 1106 Varón-González C, Pallares LF, Debat V, Navarro N. 2019. Mouse Skull Mean Shape and Shape
1107 Robustness Rely on Different Genetic Architectures and Different Loci. *Frontiers Genetics*
1108 **10**:64. doi:10.3389/fgene.2019.00064
- 1109 Vidal M, Cusick ME, Barabási A-L. 2011. Interactome Networks and Human Disease. *Cell*
1110 **144**:986–998. doi:10.1016/j.cell.2011.02.016
- 1111 Visscher PM. 2008. Sizing up human height variation. *Nat Genet* **40**:ng0508-489.
1112 doi:10.1038/ng0508-489
- 1113 Visscher PM, Wray NR, Zhang Q, Sklar P, McCarthy MI, Brown MA, Yang J. (2017). 10 Years
1114 of GWAS Discovery: Biology, Function, and Translation. *Am J Hum Genetics*. **101**:1:5-22.
1115 <https://doi.org/10.1016/j.ajhg.2017.06.005>
- 1116 Waaijenborg, S., Zwinderman, A.H. (2009) Sparse canonical correlation analysis for identifying,
1117 connecting and completing gene-expression networks. *BMC Bioinformatics* **10**, 315.
1118 <https://doi.org/10.1186/1471-2105-10-315>
- 1119 Wagner, G., Pavlicev, M., Cheverud, J. (2007). The road to modularity. *Nat Rev Genet* **8**(12),
1120 nrg2267. <https://dx.doi.org/10.1038/nrg2267>
- 1121 Wagner GP, Zhang J. 2011. The pleiotropic structure of the genotype–phenotype map: the
1122 evolvability of complex organisms. *Nat Rev Genet* **12**:204. doi:10.1038/nrg2949
- 1123 Wang K, Li M, Bucan M. 2007. Pathway-Based Approaches for Analysis of Genomewide
1124 Association Studies. *Am J Hum Genetics* **81**:1278–1283. doi:10.1086/522374
- 1125 Wang K, Li M, Hakonarson H. 2010. Analysing biological pathways in genome-wide association
1126 studies. *Nat Rev Genet* **11**:843. doi:10.1038/nrg2884
- 1127 Watson J, Francavilla C. 2018. Regulation of FGF10 Signaling in Development and Disease.
1128 *Frontiers Genetics* **9**:500. doi:10.3389/fgene.2018.00500
- 1129 Weinberg SM, Cornell R, Leslie EJ. 2018. Craniofacial genetics: Where have we been and where
1130 are we going? *Plos Genet* **14**:e1007438. doi:10.1371/journal.pgen.1007438
- 1131 White JD, Indencleef K, Naqvi S, Eller RJ, Hoskens H, Roosenboom J, Lee MK, Li J,
1132 Mohammed J, Richmond S, Quillen EE, Norton HL, Feingold E, Swigut T, Marazita ML,
1133 Peeters H, Hens G, Shaffer JR, Wysocka J, Walsh S, Weinberg SM, Shriver MD, Claes P
1134 (2021) Insights into the genetic architecture of the human face. *Nat Genet*; **53**(1):45-53.

1135 Wood AR, Esko T, Yang J, Vedantam S, Pers TH, Gustafsson S, Chu AY, Estrada K, Luan J,
 1136 Kutalik Z, Amin N, Buchkovich ML, Croteau-Chonka DC, Day FR, Duan Y, Fall T,
 1137 Fehrmann R, Ferreira T, Jackson AU, Karjalainen J, Lo KS, Locke AE, Mägi R, Mihailov E,
 1138 Porcu E, Randall JC, Scherag A, Vinkhuyzen AAE, Westra H-J, Winkler TW, Workalemahu
 1139 T, Zhao JH, Absher D, Albrecht E, Anderson D, Baron J, Beekman M, Demirkan A, Ehret
 1140 GB, Feenstra B, Feitosa MF, Fischer K, Fraser RM, Goel A, Gong J, Justice AE, Kanoni S,
 1141 Kleber ME, Kristiansson K, Lim U, Lotay V, Lui JC, Mangino M, Leach IM, Medina-Gomez
 1142 C, Nalls MA, Nyholt DR, Palmer CD, Pasko D, Pechlivanis S, Prokopenko I, Ried JS, Ripke
 1143 S, Shungin D, Stancáková A, Strawbridge RJ, Sung YJ, Tanaka T, Teumer A, Trompet S,
 1144 Laan SW van der, Setten J van, Vliet-Ostaptchouk JVV, Wang Z, Yengo L, Zhang W, Afzal
 1145 U, Ärnlöv J, Arscott GM, Bandinelli S, Barrett A, Bellis C, Bennett AJ, Berne C, Blüher M,
 1146 Bolton JL, Böttcher Y, Boyd HA, Bruinenberg M, Buckley BM, Buyske S, Caspersen IH,
 1147 Chines PS, Clarke R, Claudi-Boehm S, Cooper M, Daw EW, Jong PAD, Deelen J, Delgado G,
 1148 Denny JC, Dhonukshe-Rutten R, Dimitriou M, Doney ASF, Dörr M, Eklund N, Eury E,
 1149 Folkersen L, Garcia ME, Geller F, Giedraitis V, Go AS, Grallert H, Grammer TB, Gräßler J,
 1150 Grönberg H, Groot LCPGM de, Groves CJ, Haessler J, Hall P, Haller T, Hallmans G,
 1151 Hannemann A, Hartman CA, Hassinen M, Hayward C, Heard-Costa NL, Helmer Q, Hemani
 1152 G, Henders AK, Hillege HL, Hlatky MA, Hoffmann W, Hoffmann P, Holmen O, Houwing-
 1153 Duistermaat JJ, Illig T, Isaacs A, James AL, Jeff J, Johansen B, Johansson Å, Jolley J,
 1154 Juliusdottir T, Junttila J, Kho AN, Kinnunen L, Klopp N, Kocher T, Kratzer W, Lichtner P,
 1155 Lind L, Lindström J, Lobbens S, Lorentzon M, Lu Y, Lyssenko V, Magnusson PKE, Mahajan
 1156 A, Maillard M, McArdle WL, McKenzie CA, McLachlan S, McLaren PJ, Menni C, Merger S,
 1157 Milani L, Moayyeri A, Monda KL, Morken MA, Müller G, Müller-Nurasyid M, Musk AW,
 1158 Narisu N, Nauck M, Nolte IM, Nöthen MM, Oozageer L, Pilz S, Rayner NW, Renstrom F,
 1159 Robertson NR, Rose LM, Roussel R, Sanna S, Scharnagl H, Scholtens S, Schumacher FR,
 1160 Schunkert H, Scott RA, Sehmi J, Seufferlein T, Shi J, Silventoinen K, Smit JH, Smith AV,
 1161 Smolonska J, Stanton AV, Stirrups K, Stott DJ, Stringham HM, Sundström J, Swertz MA,
 1162 Syvänen A-C, Tayo BO, Thorleifsson G, Tyrer JP, Dijk S van, Schoor NM van, Velde N van
 1163 der, Heemst D van, Oort FVA van, Vermeulen SH, Verweij N, Vonk JM, Waite LL,
 1164 Waldenberger M, Wennauer R, Wilkens LR, Willenborg C, Wilsgaard T, Wojczynski MK,
 1165 Wong A, Wright AF, Zhang Q, Arveiler D, Bakker SJL, Beilby J, Bergman RN, Bergmann S,
 1166 Biffar R, Blangero J, Boomsma DI, Bornstein SR, Bovet P, Brambilla P, Brown MJ,
 1167 Campbell H, Caulfield MJ, Chakravarti A, Collins R, Collins FS, Crawford DC, Cupples LA,
 1168 Danesh J, Faire U de, Ruijter HM den, Erbel R, Erdmann J, Eriksson JG, Farrall M,
 1169 Ferrannini E, Ferrières J, Ford I, Forouhi NG, Forrester T, Gansevoort RT, Gejman PV,
 1170 Gieger C, Golay A, Gottesman O, Gudnason V, Gyllenstein U, Haas DW, Hall AS, Harris TB,
 1171 Hattersley AT, Heath AC, Hengstenberg C, Hicks AA, Hindorff LA, Hingorani AD, Hofman
 1172 A, Hovingh GK, Humphries SE, Hunt SC, Hypponen E, Jacobs KB, Jarvelin M-R, Jousilahti
 1173 P, Jula AM, Kaprio J, Kastelein JJP, Kayser M, Kee F, Keinänen-Kiukaanniemi SM,
 1174 Kiemeny LA, Kooner JS, Kooperberg C, Koskinen S, Kovacs P, Kraja AT, Kumari M,
 1175 Kuusisto J, Lakka TA, Langenberg C, Marchand LL, Lehtimäki T, Lupoli S, Madden PAF,
 1176 Männistö S, Manunta P, Marette A, Matise TC, McKnight B, Meitinger T, Moll FL,
 1177 Montgomery GW, Morris AD, Morris AP, Murray JC, Nelis M, Ohlsson C, Oldehinkel AJ,
 1178 Ong KK, Ouwehand WH, Pasterkamp G, Peters A, Pramstaller PP, Price JF, Qi L, Raitakari
 1179 OT, Rankinen T, Rao DC, Rice TK, Ritchie M, Rudan I, Salomaa V, Samani NJ, Saramies J,
 1180 Sarzynski MA, Schwarz PEH, Sebert S, Sever P, Shuldiner AR, Sinisalo J, Steinthorsdottir V,

- 1181 Stolk RP, Tardif J-C, Tönjes A, Tremblay A, Tremoli E, Virtamo J, Vohl M-C, Consortium
1182 TEMR and G (eMERGE), Consortium TMig, Consortium TP, Study TLC, Amouyel P,
1183 Asselbergs FW, Assimes TL, Bochud M, Boehm BO, Boerwinkle E, Bottinger EP, Bouchard
1184 C, Cauchi S, Chambers JC, Chanock SJ, Cooper RS, Bakker PIW de, Dedoussis G, Ferrucci
1185 L, Franks PW, Froguel P, Groop LC, Haiman CA, Hamsten A, Hayes MG, Hui J, Hunter DJ,
1186 Hveem K, Jukema JW, Kaplan RC, Kivimaki M, Kuh D, Laakso M, Liu Y, Martin NG, März
1187 W, Melbye M, Moebus S, Munroe PB, Njølstad I, Oostra BA, Palmer CNA, Pedersen NL,
1188 Perola M, Pérusse L, Peters U, Powell JE, Power C, Quertermous T, Rauramaa R, Reinmaa E,
1189 Ridker PM, Rivadeneira F, Rotter JI, Saaristo TE, Saleheen D, Schlessinger D, Slagboom PE,
1190 Snieder H, Spector TD, Strauch K, Stumvoll M, Tuomilehto J, Uusitupa M, Harst P van der,
1191 Völzke H, Walker M, Wareham NJ, Watkins H, Wichmann H-E, Wilson JF, Zanen P,
1192 Deloukas P, Heid IM, Lindgren CM, Mohlke KL, Speliotes EK, Thorsteinsdottir U, Barroso I,
1193 Fox CS, North KE, Strachan DP, Beckmann JS, Berndt SI, Boehnke M, Borecki IB,
1194 McCarthy MI, Metspalu A, Stefansson K, Uitterlinden AG, Duijn CM van, Franke L, Willer
1195 CJ, Price AL, Lettre G, Loos RJF, Weedon MN, Ingelsson E, O'Connell JR, Abecasis GR,
1196 Chasman DI, Goddard ME, Visscher PM, Hirschhorn JN, Frayling TM. 2014. Defining the
1197 role of common variation in the genomic and biological architecture of adult human height.
1198 *Nat Genet* **46**:ng.3097. doi:10.1038/ng.3097
- 1199 Wray NR, Goddard ME, Visscher PM. 2007. Prediction of individual genetic risk to disease
1200 from genome-wide association studies. *Genome Res* **17**:1520–1528. doi:10.1101/gr.6665407
- 1201 Wray NR, Yang J, Hayes BJ, Price AL, Goddard ME, Visscher PM. 2013. Pitfalls of predicting
1202 complex traits from SNPs. *Nat Rev Genet* **14**:nrg3457. doi:10.1038/nrg3457
- 1203 Xiong, Z., Dankova, G., Howe, L. J., Lee, M. K., Hysi, P. G., de Jong, M. A., . . . Kayser, M.
1204 (2019). Novel genetic loci affecting facial shape variation in humans. *Elife*, 8, e49898.
1205 doi:10.7554/eLife.49898
- 1206 Yang, J., Benyamin, B., McEvoy, B. P., Gordon, S., Henders, A. K., Nyholt, D. R., Madden, P.
1207 A., Heath, A. C., Martin, N. G., Montgomery, G. W., Goddard, M. E., & Visscher, P. M.
1208 (2010). Common SNPs explain a large proportion of the heritability for human height. *Nat*
1209 *Genet*, **42**(7), 565-569. doi:ng.608
- 1210 Andrew D Yates, Premanand Achuthan, Wasiu Akanni, James Allen, Jamie Allen, Jorge
1211 Alvarez-Jarreta, M Ridwan Amode, Irina M Armean, Andrey G Azov, Ruth Bennett, Jyothish
1212 Bhai, Konstantinos Billis, Sanjay Boddu, José Carlos Marugán, Carla Cummins, Claire
1213 Davidson, Kamalkumar Dodiya, Reham Fatima, Astrid Gall, Carlos Garcia Giron, Laurent
1214 Gil, Tiago Grego, Leanne Haggerty, Erin Haskell, Thibaut Hourlier, Osagie G Izuogu, Sophie
1215 H Janacek, Thomas Juettemann, Mike Kay, Ilias Lavidas, Tuan Le, Diana Lemos, Jose
1216 Gonzalez Martinez, Thomas Maurel, Mark McDowall, Aoife McMahon, Shamika Mohanan,
1217 Benjamin Moore, Michael Nuhn, Denye N Oheh, Anne Parker, Andrew Parton, Mateus
1218 Patricio, Manoj Pandian Sakthivel, Ahamed Imran Abdul Salam, Bianca M Schmitt, Helen
1219 Schuilenburg, Dan Sheppard, Mira Sycheva, Marek Szuba, Kieron Taylor, Anja Thormann,
1220 Glen Threadgold, Alessandro Vullo, Brandon Walts, Andrea Winterbottom, Amonida Zadissa,
1221 Marc Chakiachvili, Bethany Flint, Adam Frankish, Sarah E Hunt, Garth Iisley, Myrto

- 1222 Kostadima, Nick Langridge, Jane E Loveland, Fergal J Martin, Joannella Morales, Jonathan
 1223 M Mudge, Matthieu Muffato, Emily Perry, Magali Ruffier, Stephen J Trevanion, Fiona
 1224 Cunningham, Kevin L Howe, Daniel R Zerbino, Paul Flicek, Ensembl (2020). *Nucleic Acids*
 1225 *Research*, **48**, D1, D682–D688, <https://doi.org/10.1093/nar/gkz966>
- 1226 Yoon BS, Ovchinnikov DA, Yoshii I, Mishina Y, Behringer RR, Lyons KM. 2005. Bmpr1a and
 1227 Bmpr1b have overlapping functions and are essential for chondrogenesis in vivo. *P Natl Acad*
 1228 *Sci Usa* **102**:5062–5067. doi:10.1073/pnas.0500031102
- 1229 Young NM, Chong HJ, Hu D, Hallgrímsson B, Marcucio RS. 2010. Quantitative analyses link
 1230 modulation of sonic hedgehog signaling to continuous variation in facial growth and shape.
 1231 *Development* **137**:3405–3409. doi:10.1242/dev.052340
- 1232 Yue F, Cheng Y, Breschi A, Vierstra J, Wu W, Ryba T, Sandstrom R, Ma Z, Davis C, Pope BD,
 1233 Shen Y, Pervouchine DD, Djebali S, Thurman RE, Kaul R, Rynes E, Kirilusha A, Marinov
 1234 GK, Williams BA, Trout D, Amrhein H, Fisher-Aylor K, Antoshechkin I, DeSalvo G, See L-
 1235 H, Fastuca M, Drenkow J, Zaleski C, Dobin A, Prieto P, Lagarde J, Bussotti G, Tanzer A,
 1236 Denas O, Li K, Bender MA, Zhang M, Byron R, Groudine MT, McCleary D, Pham L, Ye Z,
 1237 Kuan S, Edsall L, Wu Y-C, Rasmussen MD, Bansal MS, Kellis M, Keller CA, Morrissey CS,
 1238 Mishra T, Jain D, Dogan N, Harris RS, Cayting P, Kawli T, Boyle AP, Euskirchen G,
 1239 Kundaje A, Lin S, Lin Y, Jansen C, Malladi VS, Cline MS, Erickson DT, Kirkup VM,
 1240 Learned K, Sloan CA, Rosenbloom KR, Sousa BL de, Beal K, Pignatelli M, Flicek P, Lian J,
 1241 Kahveci T, Lee D, Kent WJ, Santos MR, Herrero J, Notredame C, Johnson A, Vong S, Lee K,
 1242 Bates D, Neri F, Diegel M, Canfield T, Sabo PJ, Wilken MS, Reh TA, Giste E, Shafer A,
 1243 Kutyavin T, Haugen E, Dunn D, Reynolds AP, Neph S, Humbert R, Hansen RS, Bruijn MD,
 1244 Selleri L, Rudensky A, Josefowicz S, Samstein R, Eichler EE, Orkin SH, Levasseur D,
 1245 Papayannopoulou T, Chang K-H, Skoultschi A, Gosh S, Disteche C, Treuting P, Wang Y,
 1246 Weiss MJ, Blobel GA, Cao X, Zhong S, Wang T, Good PJ, Lowdon RF, Adams LB, Zhou X-
 1247 Q, Pazin MJ, Feingold EA, Wold B, Taylor J, Mortazavi A, Weissman SM,
 1248 Stamatoyannopoulos JA, Snyder MP, Guigo R, Gingeras TR, Gilbert DM, Hardison RC, Beer
 1249 MA, Ren B, Consortium TME. 2014. A comparative encyclopedia of DNA elements in the
 1250 mouse genome. *Nature* **515**:355. doi:10.1038/nature13992
- 1251 ZHAO, M., HARRIS, S.E., HORN, D., GENG, Z., NISHIMURA, R., MUNDY, G.R. and
 1252 CHEN, D. (2002). Bone morphogenetic protein receptor signaling is necessary for normal
 1253 murine postnatal bone formation. *J Cell Biol* **157**: 1049-60.

1254

1255

1256

1257 **Figure legends**

1258 Figure 1. Process MGP schematic. Once a process is selected, we cross-reference the known
 1259 gene locations using Ensembl with the locations of the genotyped markers in the DO sample.
 1260 The founder probabilities of the nearest upstream and downstream markers are averaged for each

gene. The compiled founder probabilities and landmark coordinates are then used in a regularized PLS model to estimate the axis of greatest covariance between the marker data and craniofacial variation.

Figure 2. Process MGP for chondrocyte differentiation with a regularization parameter of .075. A) PLS1 genetic loadings are shown for each gene in the model sorted from largest to smallest effects. Individual founder allele effect sizes are colored within each bar. The gene in red text corresponds to the mutant used for comparison of phenotypic effects. B) The estimated chondrocyte differentiation MGP phenotype is shown with a heatmap. Warm colors represent areas of relative expansion, light green represents areas of little shape effect, and cool colors represent areas with relative contraction. C) Chondrocyte differentiation MGP effects shown in black vectors multiplied 4x are compared to a *Bmpr1b* (*Alk6*) homozygous mutant is shown with red vectors. The vector correlation between chondrocyte differentiation MGP and *Bmpr1b* is shown below the phenotypic effects.

Figure 2—figure supplement 1. 10-fold cross validation results for the chondrocyte differentiation MGP. The black-labelled Y axis on the left shows the vector correlation between the process MGP model and a *Bmpr1b* mutant. The red-labelled Y axis on the right shows the root mean squared error (RMSE) of the out-of-fold phenotypic prediction. The X axis shows the range of regularization strengths for the PLS model. The regularization parameter was chosen to balance the minimization of RMSE and the maximization of the vector correlation to *Bmpr1b*. The chosen parameter is shown as a black tick along the X axis.

Figure 2—figure supplement 2. Permutation of marker sets of fixed size. The permuted R^2 distribution of 10000 chondrocyte differentiation MGP analyses is shown in blue. The estimated R^2 of the chondrocyte differentiation MGP is shown as a black vertical line.

Figure 3. Chondrocyte defects in *Bmpr1b* mutants. A-B) Quantification of cell size in the sections of the intersphenoid synchondrosis shows an increase in relative cell size as well as a change in the distribution of cell sizes throughout the width of the synchondrosis. C) Sections of intersphenoid synchondroses highlighting the midline and extremes of the synchondroses. D) Premature fusion of the coronal suture is visible in *Bmpr1b* homozygous mutants.

Figure 3—figure supplement 1. Chondrocyte morphometric example. Landmarks are placed in the top, bottom, left, and right sides of the cell to best capture the height and width of the cells (show here as crosses). The height and width measurements are then used to calculate the area of an ellipsoid as an approximation of cell size.

Figure 4. Process MGP for determination of left/right symmetry with a regularization parameter of .04. A) PLS1 genetic loadings are shown for each gene in the model sorted from largest to smallest effects. Individual founder allele effect sizes are colored within each bar. The gene in red text corresponds to the mutant used for comparison of phenotypic effects. B) The estimated left/right symmetry MGP phenotype is shown with a heatmap. Warm colors represent areas of relative expansion, light green represents areas of little shape effect, and cool colors represent areas with relative contraction. C) Estimated left/right symmetry MGP phenotype is shown with

black vectors multiplied 4x. An *Fgf10* homozygous mutant is shown with red vectors for comparison. The vector correlation between left/right symmetry MGP and the *Fgf10* mutant is shown below the phenotypic effects. D) Visualizations of asymmetry in the L/R MGP response and the *Fgf10* homozygous mutant. Asymmetry vectors are magnified 4x.

Figure 4—figure supplement 1. 10-fold cross validation results for the chondrocyte differentiation MGP. The black-labelled Y axis on the left shows the vector correlation between the process MGP model and a *Fgf10* homozygous mutant. The red-labelled Y axis on the right shows the root mean squared error (RMSE) of the out-of-fold phenotypic prediction. The X axis shows the range of regularization strengths for the PLS model. The regularization parameter was chosen to balance the minimization of RMSE and the maximization of the vector correlation to the *Fgf10* homozygous mutant. The chosen parameter is shown as a black tick along the X axis.

Figure 4—figure supplement 2. The permuted R^2 distribution of 10000 L/R symmetry MGP analyses is shown in blue. The estimated R^2 of L/R symmetry MGP is shown as a black vertical line.

Figure 5. Process MGP for palate development. A) PLS1 genetic loadings are shown for each gene in the model sorted from largest to smallest effects. Individual founder allele effect sizes are colored within each bar. The gene in red text corresponds to the mutant used for comparison of phenotypic effects. B) The estimated palate development MGP phenotype is shown with a heatmap. Warm colors represent areas of relative expansion, light green represents areas of little shape effect, and cool colors represent areas with relative contraction. C) Estimated palate development MGP phenotype is shown with black vectors multiplied 4x. An *Ankrd11* mutant mean is shown with red vectors for comparison. The vector correlation between palate development MGP and the *Ankrd11* mutant is shown below the phenotypic effects.

Figure 5—figure supplement 1. 10-fold cross validation results for the palate development MGP. The black-labelled Y axis on the left shows the vector correlation between the process MGP model and a *Ankrd11* homozygous mutant. The red-labelled Y axis on the right shows the root mean squared error (RMSE) of the out-of-fold phenotypic prediction. The X axis shows the range of regularization strengths for the PLS model. The regularization parameter was chosen to balance the minimization of RMSE and the maximization of the vector correlation to the *Ankrd11* heterozygous mutant. The chosen parameter is shown as a black tick along the X axis.

Figure 5—figure supplement 2. The permuted R^2 distribution of 10000 palate development MGP analyses is shown in blue. The estimated R^2 of palate development MGP is shown as a black vertical line.

Figure 6. Gene drop tests. For each of the example analyses, we show the effect of removing the most heavily loaded markers from the Process MGP analysis on the A) variance explained by the model and B) vector correlation with the full model. The variance explained as well as vector correlation is relatively stable for both L/R symmetry and Palate development MGP models, suggesting that the effect is driven by the coordination of many markers. In contrast, Chondrocyte differentiation MGP shows large differences, particularly in the direction of the phenotypic effect as the most heavily loaded markers are removed from the analysis.

Figure 6—figure supplement 1. Single marker importance. For a sample of 500 processes, we show the proportion of processes with a single marker with .5, 2, and 3 times higher effect size than any other marker. 51.6% of processes show a marker effect .5 times larger than any other individual effect. 36.6% of processes show a marker effect 2 times larger than any other individual effect. 20% of processes show a marker effect 3 times larger than any other individual effect.

Figure 7. Pairwise MGP vector correlations A) Pairwise correlations of phenotypic effects for 15 process MGP analyses. Scale on the right denotes color correspondences to vector correlation, where yellows are high correlations, greens are moderate, and blues are low. B) Pairwise process MGP vector correlations as a function of the number of shared genes between the processes. Processes that share less than 10 genes can produce very similar and very disparate phenotypic effects. Processes with substantial numbers of shared genes will tend to show highly correlated responses as they increasingly use similar marker sets.

Figure 7—figure supplement 1. Pairwise process MGP vector correlations as a function of the number of shared genes between the processes. The pairwise vector comparisons have been subset to only include the processes shown in Figure 7A, with four pairs highlighted. Processes that share less than 10 genes can produce very similar and very disparate phenotypic effects. Processes with substantial numbers of shared genes will tend to show highly correlated responses as they increasingly use similar marker sets.

Figure 8. Comparisons of MGP and mouse mutant directions. A) Seven MGP phenotypes projected onto a PCA of the DO and a sample of 30 mutant mouse genotypes. Mutant means are labeled in black. The directions of MGP effects are shown with orange vectors from the DO mean to the associated process MGP. The range of DO variation on PCs 1 and 2 is shown with the shaded ellipse with an orange border. B) A heatmap of vector correlations between 30 mutant effects and 30 process MGP effects. The scale on the right denotes color correspondences to vector correlation, where yellows are high correlations, greens are moderate, and blues are low.

Figure 9. Example screenshot of web version of process analysis. Analyses include a barplot of the relative effect sizes of each selected marker and the associated phenotype shown with black vectors at each landmark. If a mutant comparison is selected, the vector correlation is provided and the mutant phenotype is shown with red vectors. Selecting “send me the results” generates an HTML report with an interactive 3D model.

Figure 9—figure supplement 1. Combining queries in the MGP shiny app with the pipe operator. In order to filter the GO database with multiple terms, the pipe operator can be used as shown. Here, the user has selected processes associated with either the apoptosis or Wnt pathway process. The barplot shows the relative effect sizes for markers associated to both “Wnt signaling pathway” and “execution phase of apoptosis” GO terms.

Figure 10. 54 3D landmark configuration. A) Sagittal view of representative scan with landmarks shown as red spheres. B) Dorsal view of landmark configuration. C) Ventral view of landmark configuration.

Figure 10—figure supplement 1. Demographic plots for the DO sample. A) The distribution of the sample by generation and data source (lab). B) Distribution of sex by source (lab).

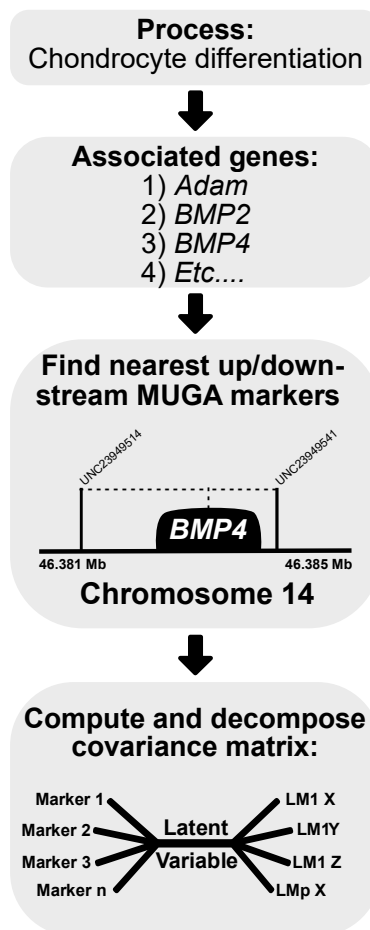


Figure 1

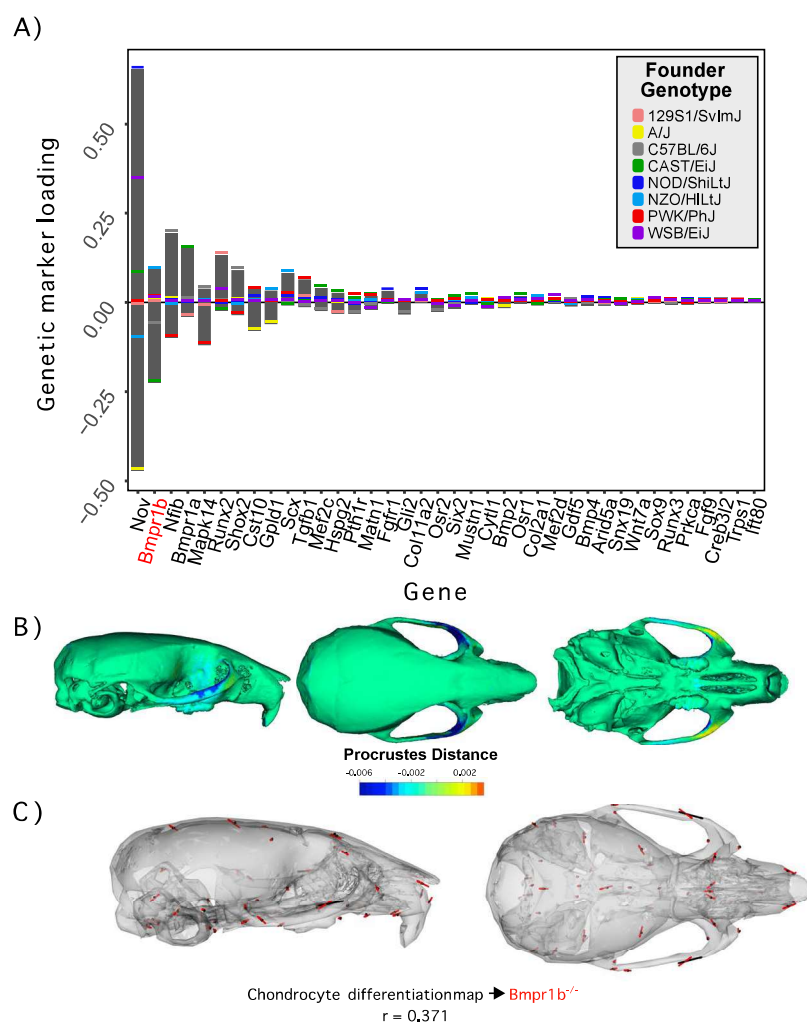


Figure 2

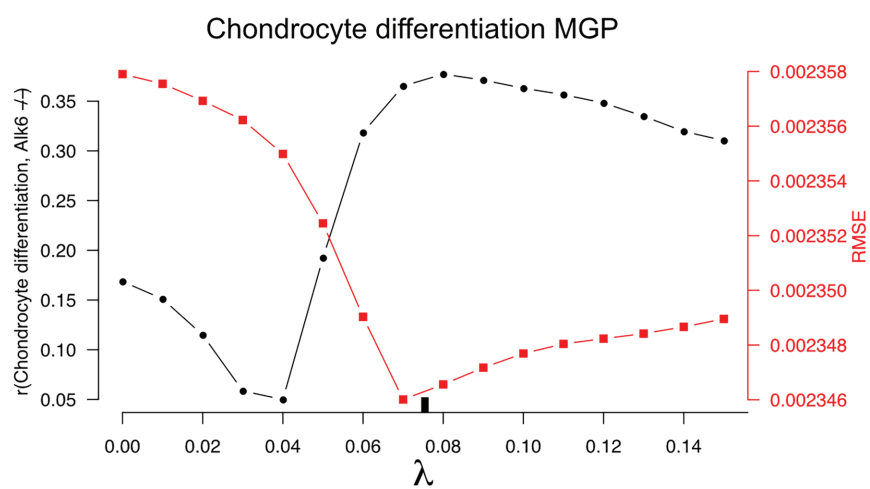


Figure Supplement - Figure 2, figure supplement 1

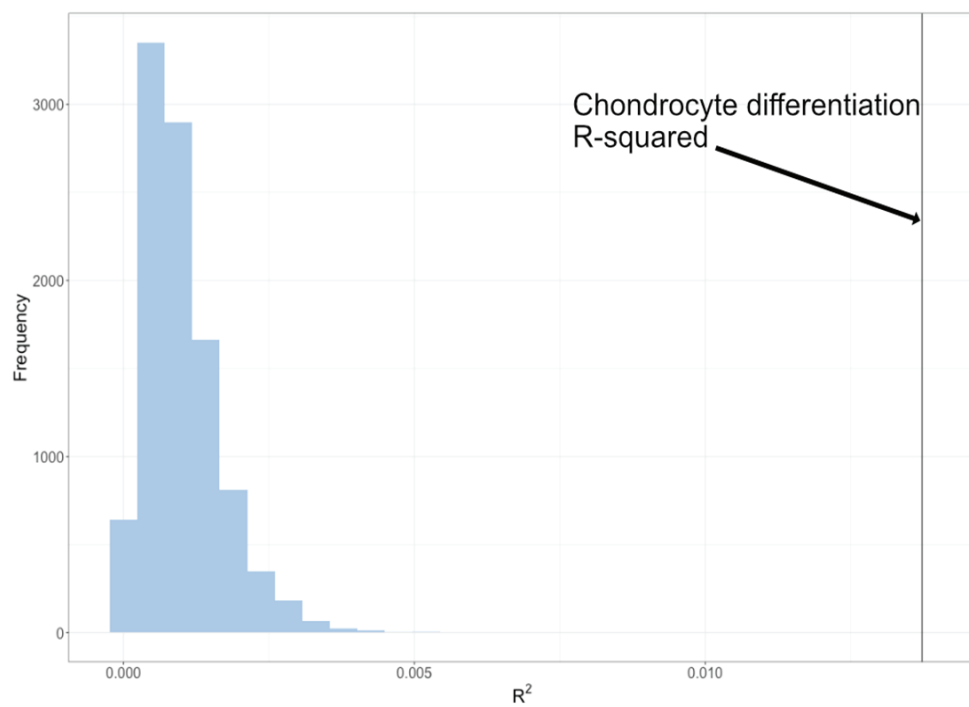


Figure 2 - figure supplement 2

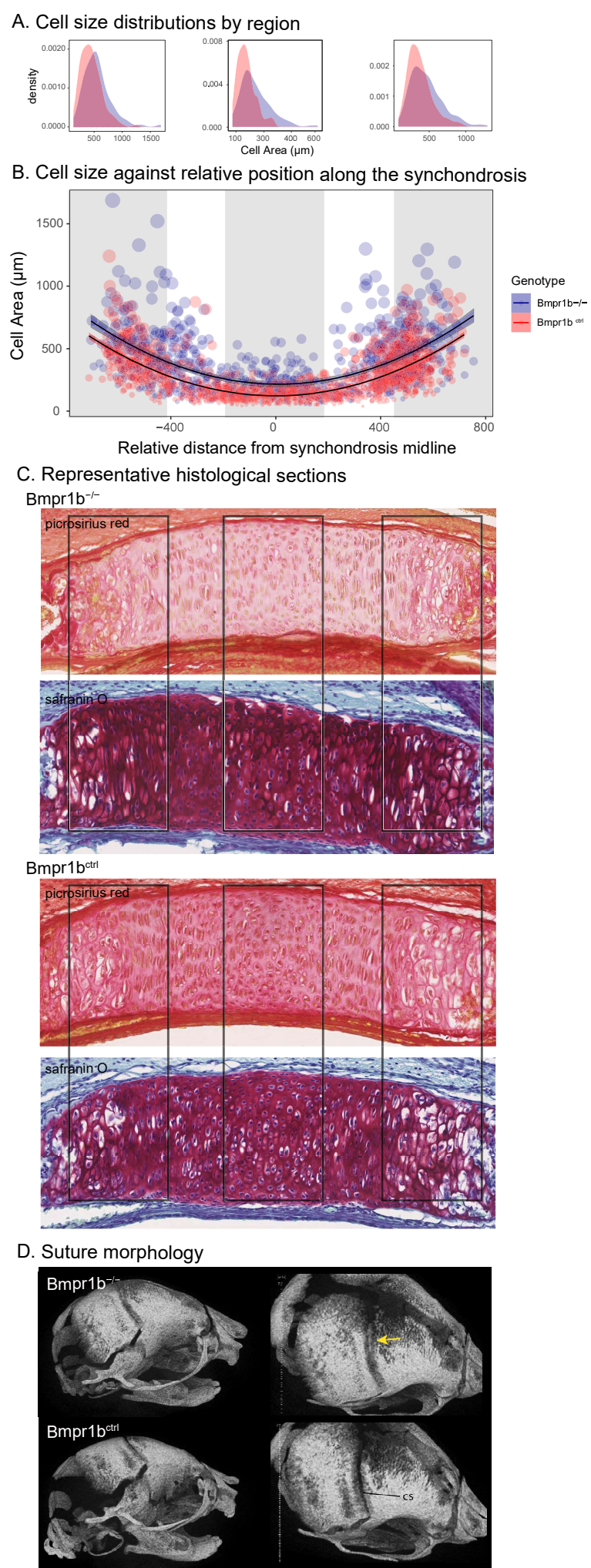


Figure 3

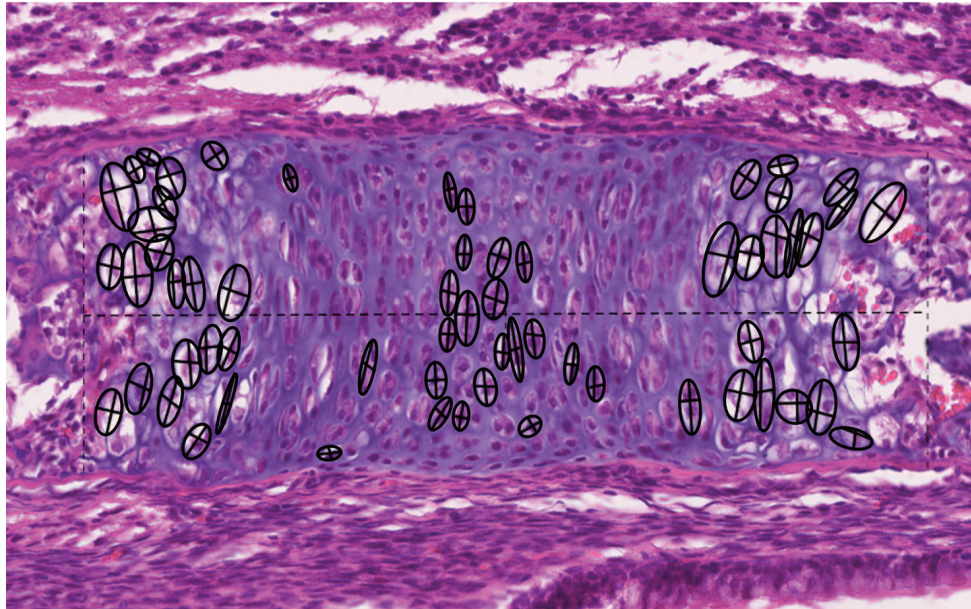


Figure 3 - Figure supplement 1

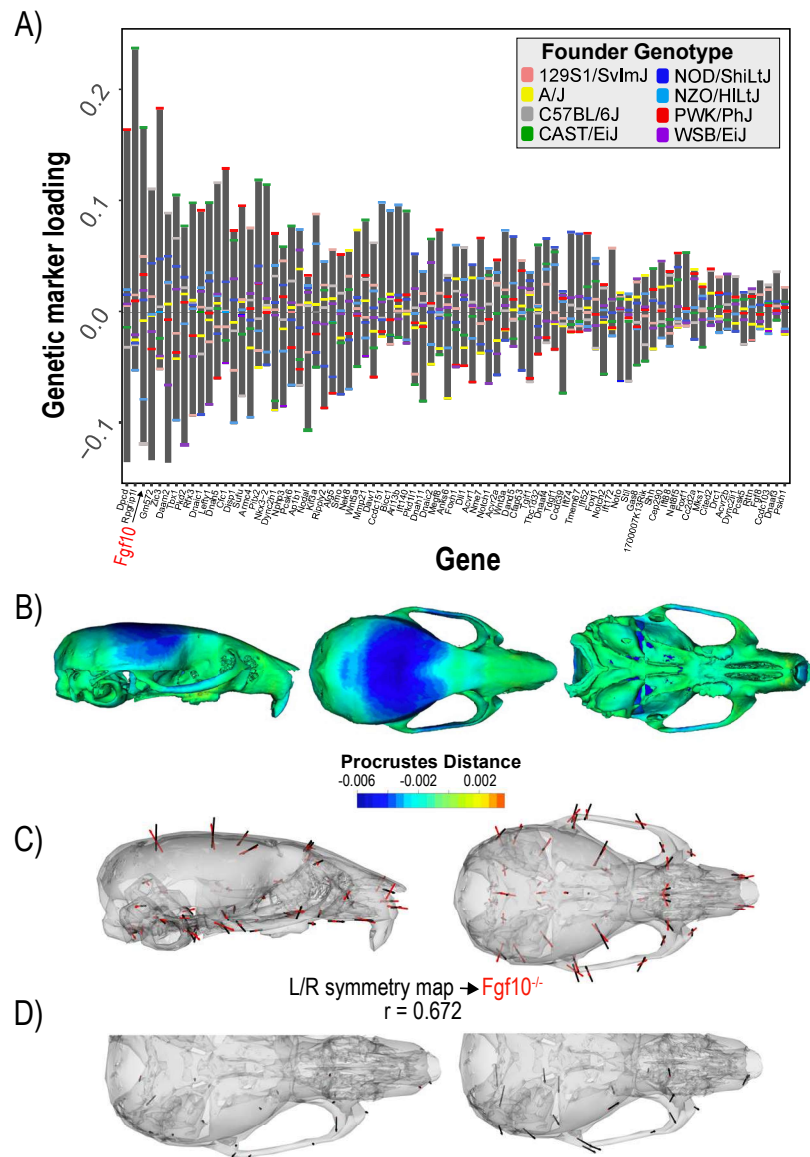


Figure 4

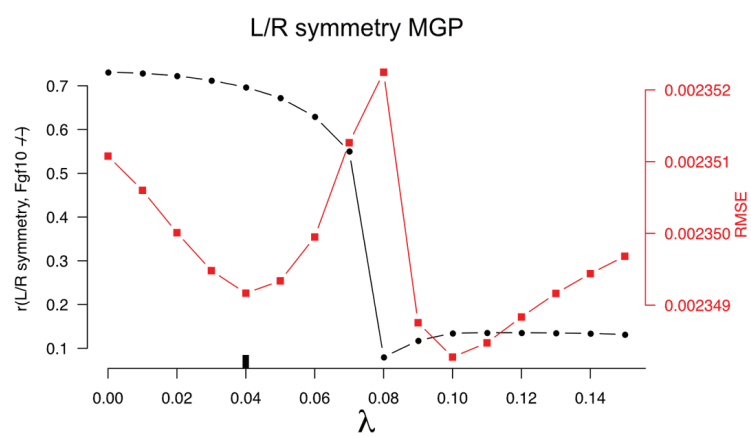


Figure 4 - figure supplement 1

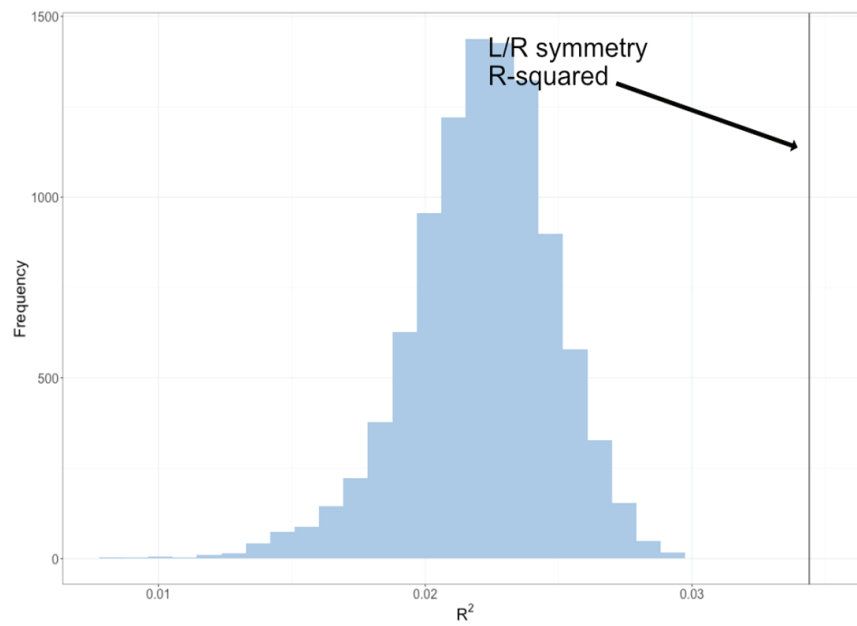


Figure 4 - figure supplement 2

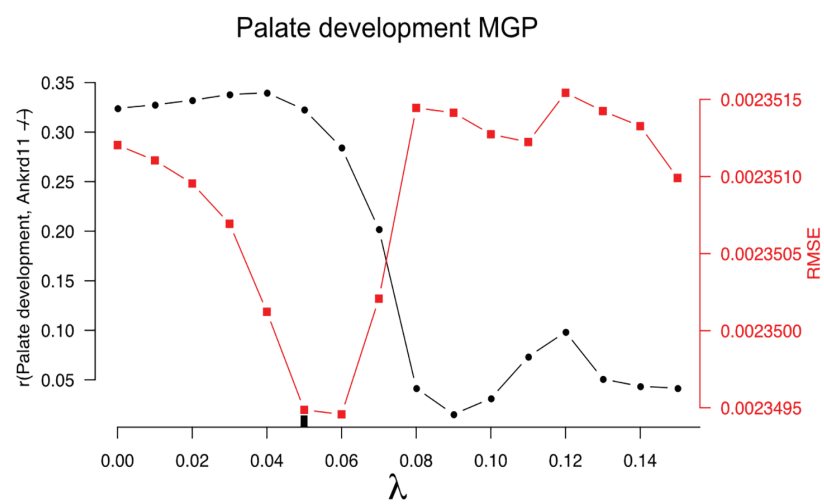


Figure 5 - figure supplement 1

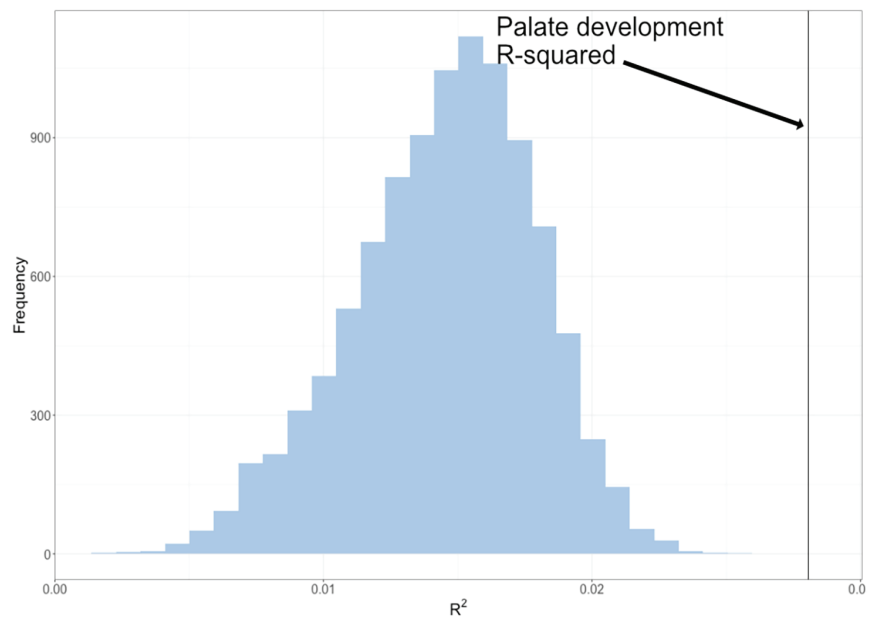


Figure 5 - figure supplement 2

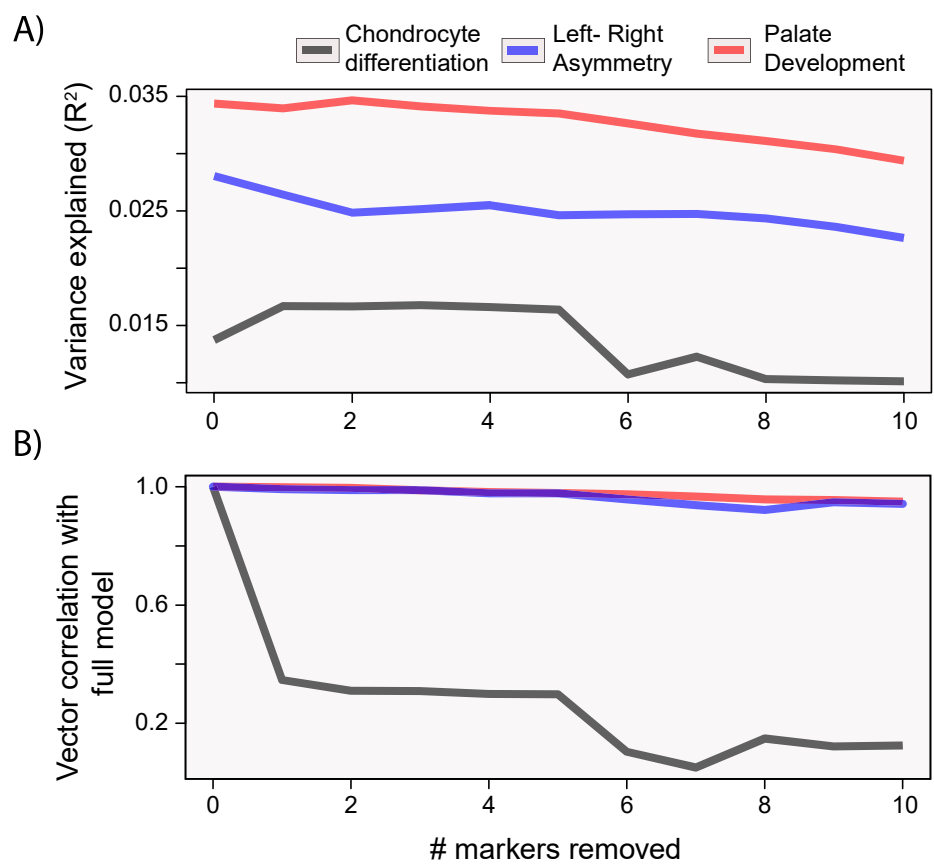


Figure 6

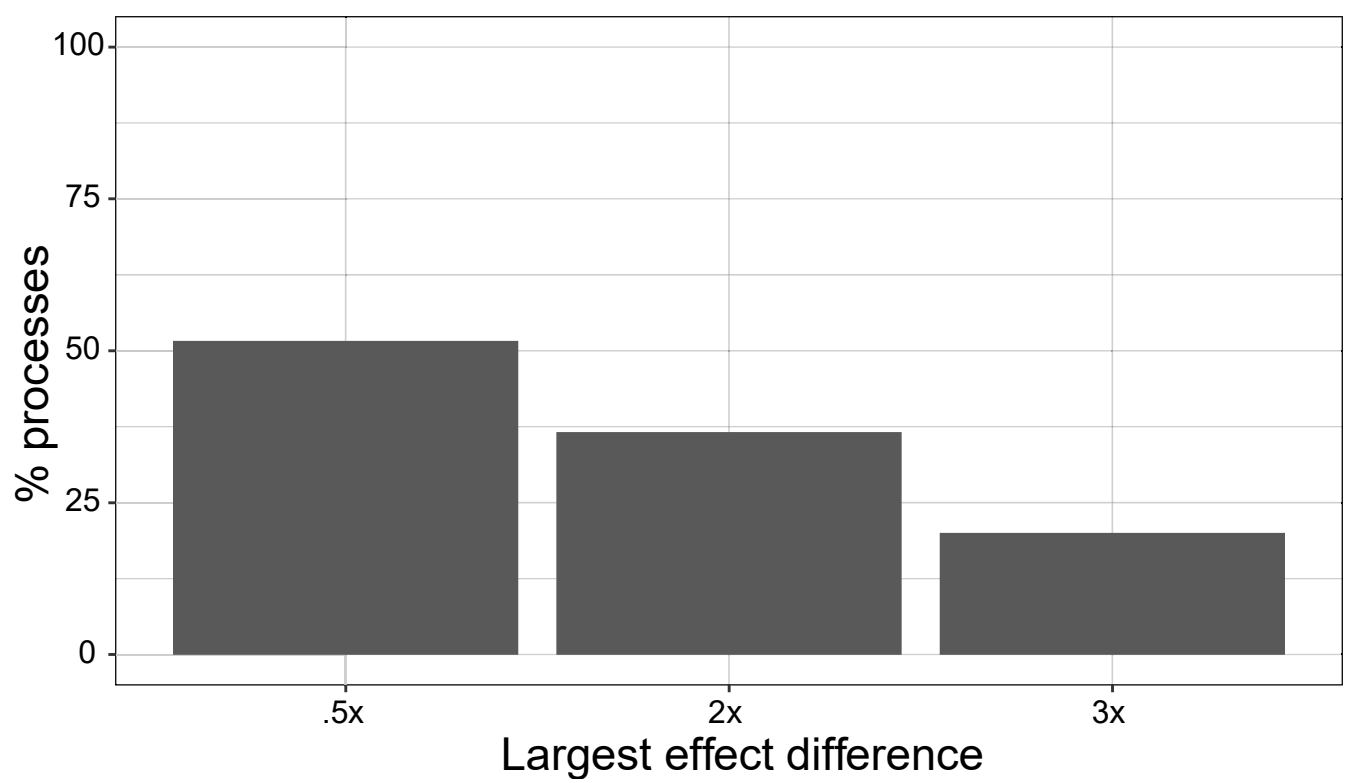
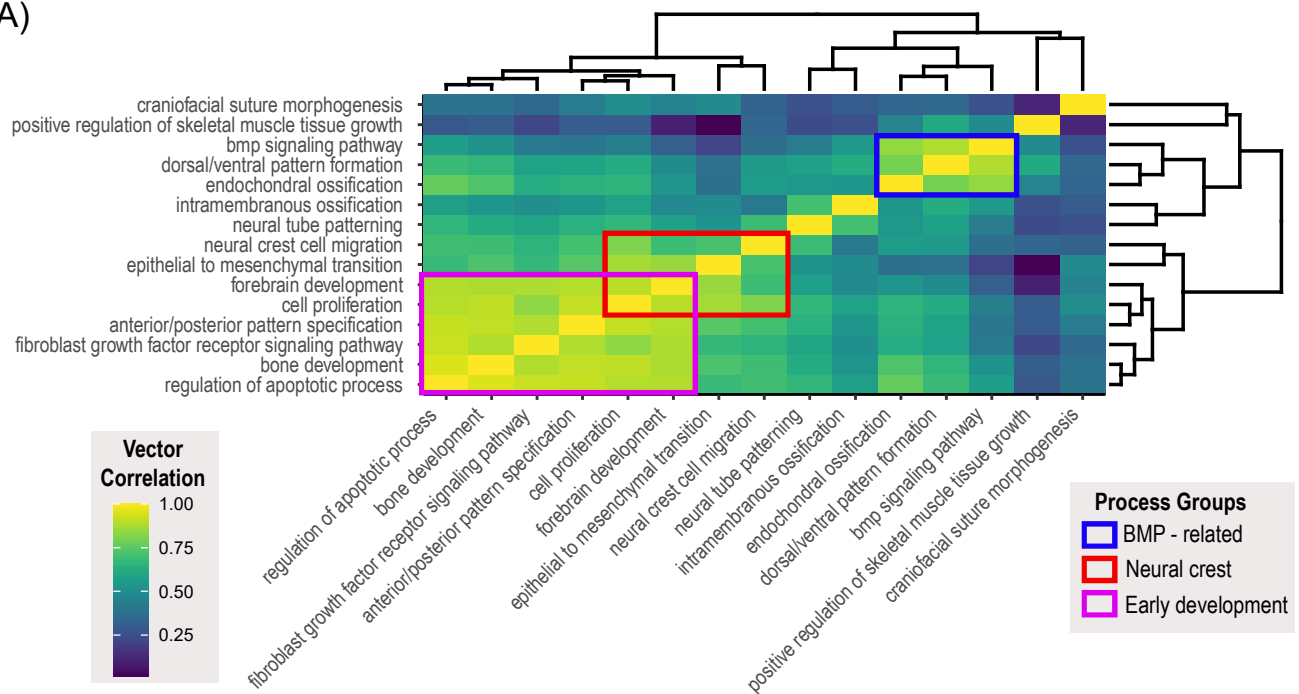


Figure 6 figure supplement 1

A)



B)

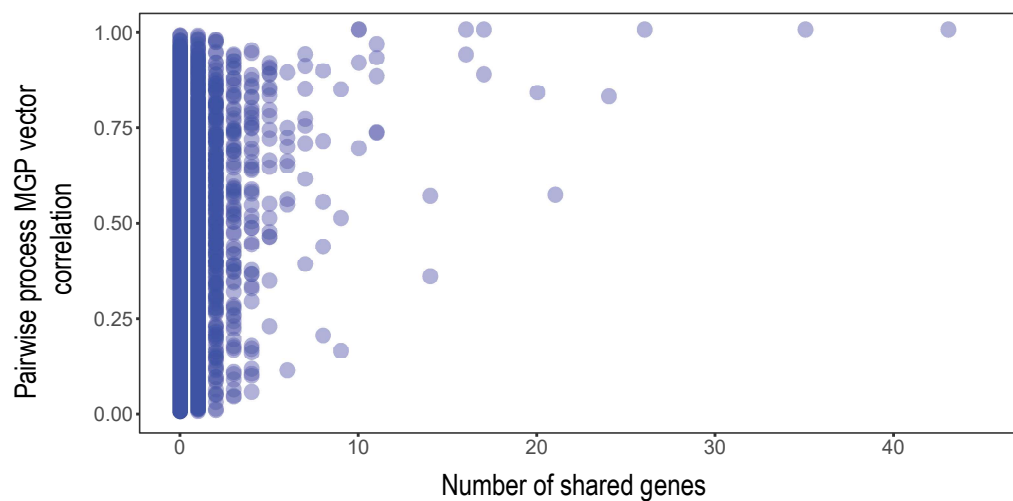


Figure 7

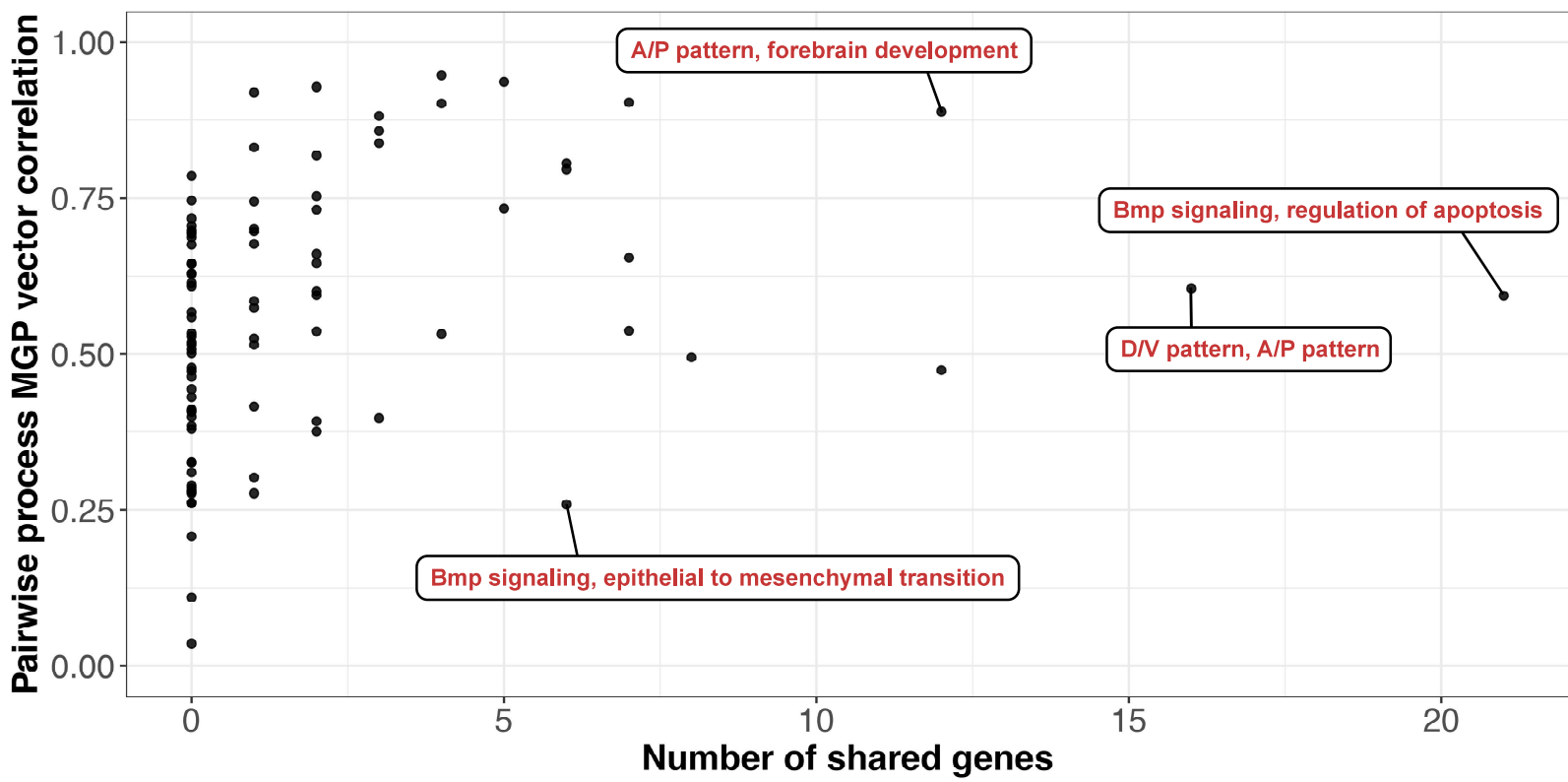


Figure 7 supplement 1

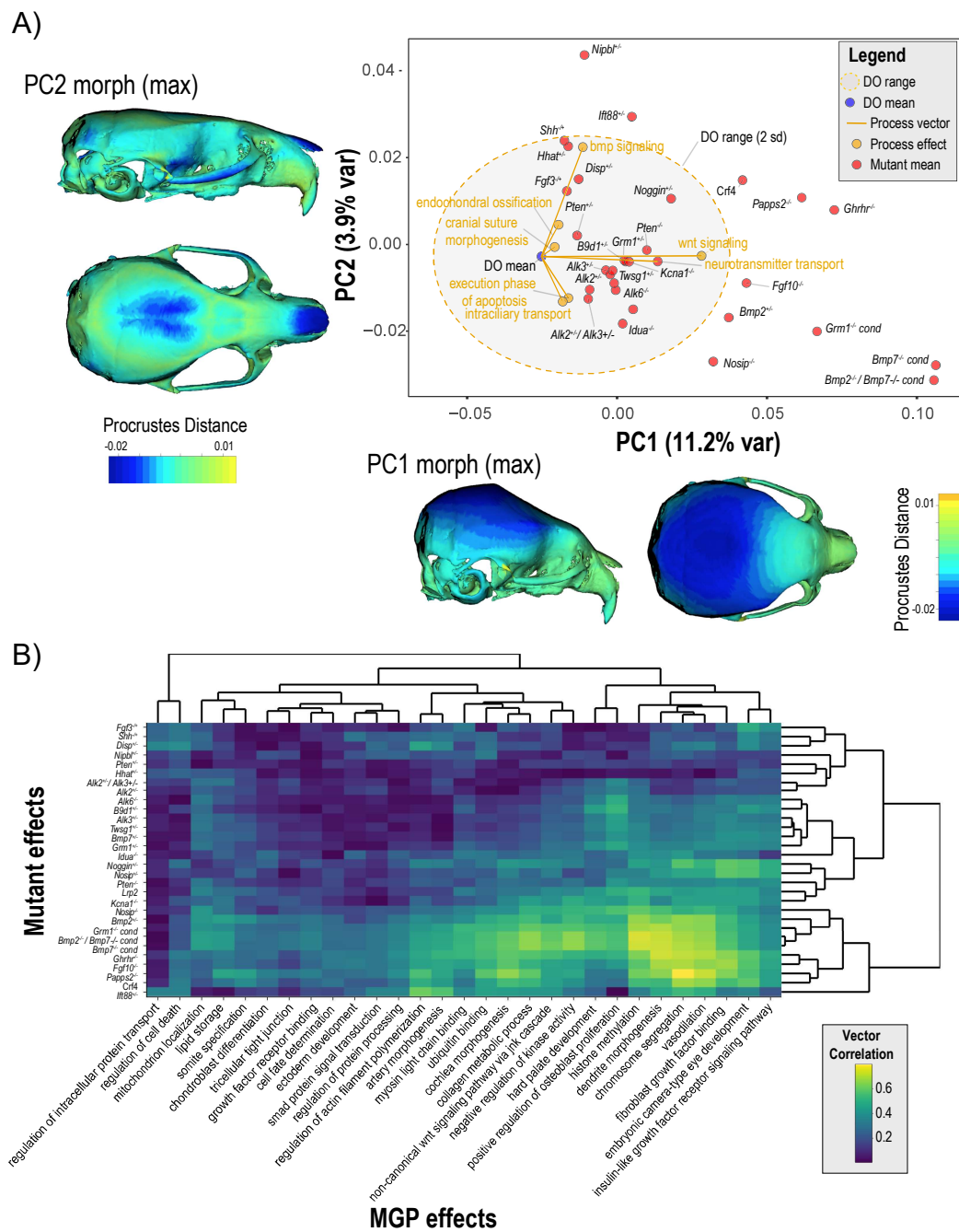


Figure 8

Process

Process filter

Type of plot

Magnification

Sparsity parameter

PLS axis

Make a comparison?

[Send me the results!](#)

[Update process!](#)

Process MGP Custom MGP Recent searches About this app

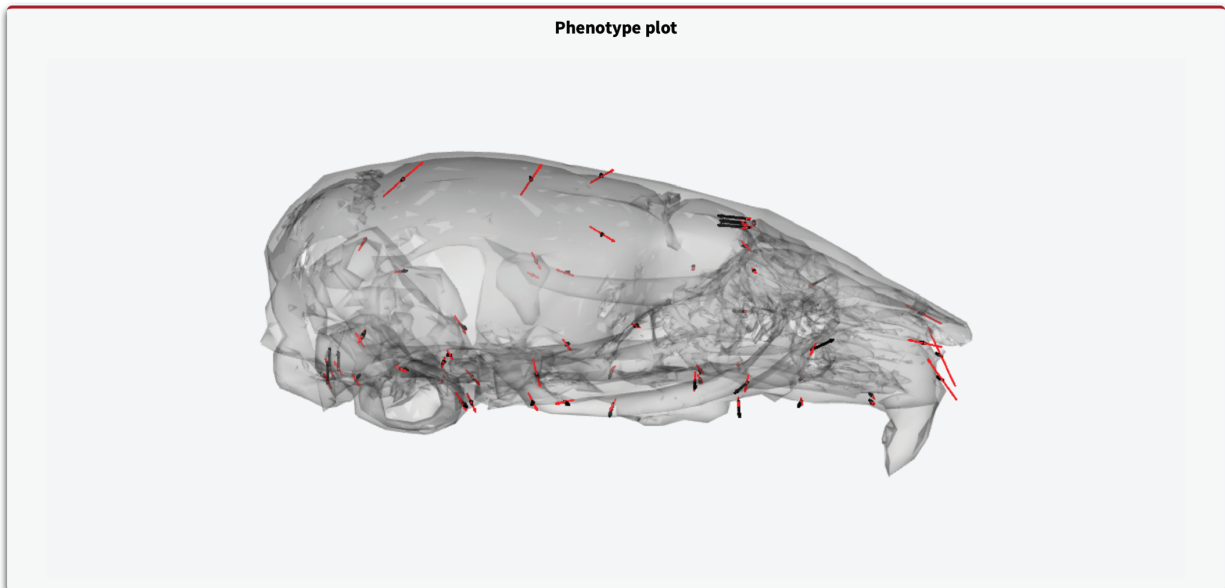
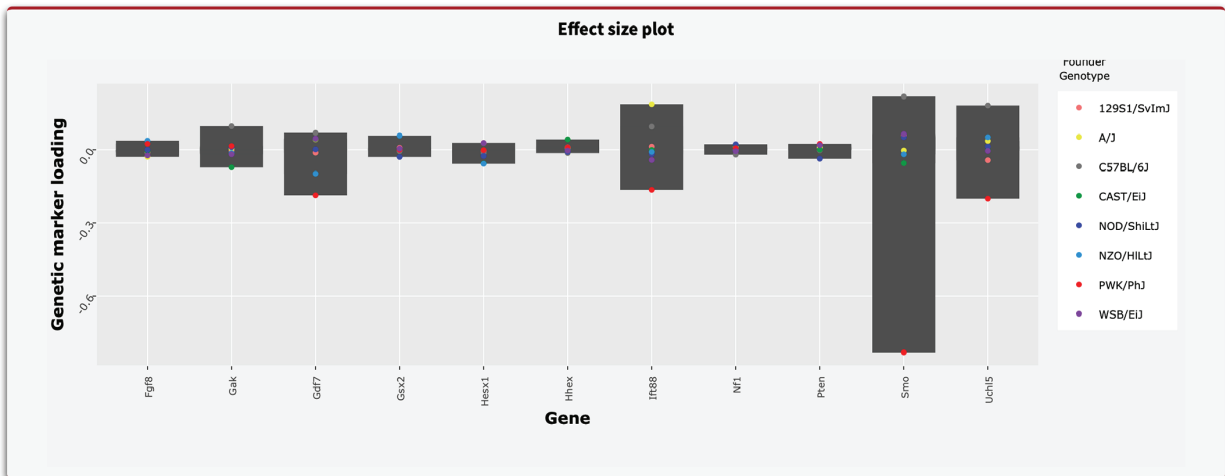


Figure 9

Wnt signaling pathway, execution phase of apoptosis MGP

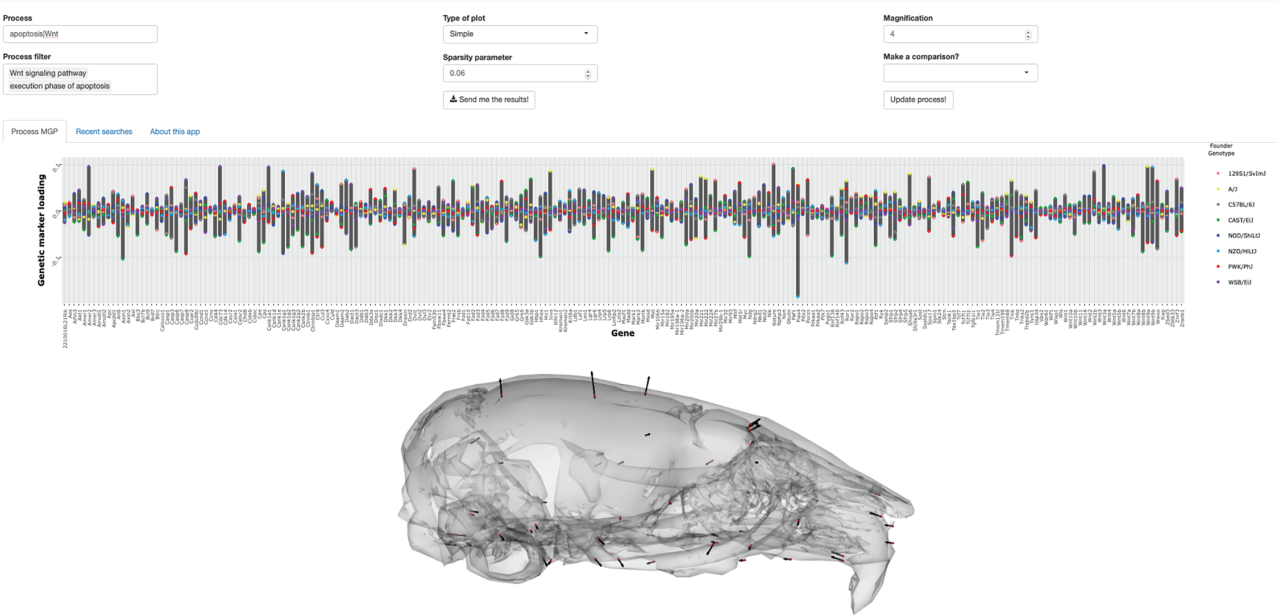


Figure 9 supplement 1

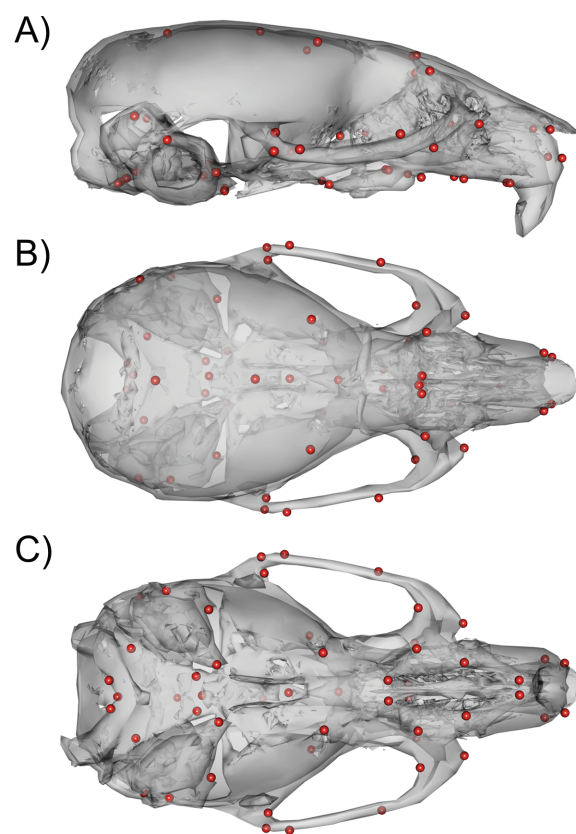
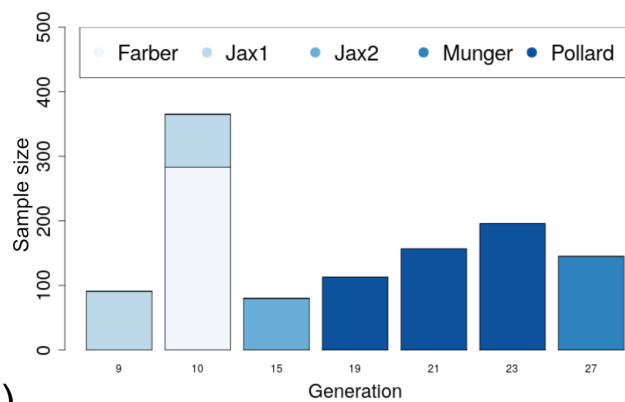


Figure 10

A)



B)

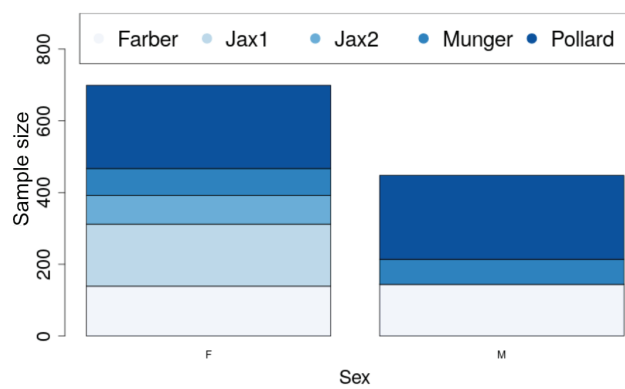


Figure 10 supplement 1